


RESEARCH ARTICLE

Size matters: Biomolecular compositions of small and large extracellular vesicles in the urine of glioblastoma patients

Susannah M. Hallal^{1,2,3} | Liam A. Sida³ | Csilla Ágota Túzesi^{2,3} | Brindha Shivalingam^{1,4,5} | Hao-Wen Sim^{6,7,8}  | Michael E. Buckland^{2,3} | Laveniya Satgunaseelan^{1,2,5} | Kimberley L. Alexander^{1,2,3} 

¹Neurosurgery Department, Chris O'Brien Lifehouse, Camperdown, NSW, Australia

²Department of Neuropathology, Royal Prince Alfred Hospital, Camperdown, NSW, Australia

³School of Medical Sciences, The University of Sydney, Camperdown, NSW, Australia

⁴Neurosurgery Department, Royal Prince Alfred Hospital, Camperdown, NSW, Australia

⁵Sydney Medical School, Faculty of Medicine and Health Sciences, The University of Sydney, Camperdown, NSW, Australia

⁶Department of Medical Oncology, Chris O'Brien Lifehouse, Camperdown, NSW, Australia

⁷NHMRC Clinical Trials Centre, The University of Sydney, Camperdown, NSW, Australia

⁸Faculty of Medicine and Health, University of New South Wales, Kensington, NSW, Australia

Correspondence

Dr. Kimberley L. Alexander, Brain Cancer Research, Chris O'Brien Lifehouse, 119-143 Missenden Road
Camperdown NSW 2050, PO BOX M33
Missenden Road, NSW 2050, Australia. Email: Kim.Alexander@lh.org.au

Funding information

SurFebruary Cancer Research Fund; Sydney Research (Sydney Cancer Institute Seed Grant); Tour de Cure, Grant/Award Number: (RSP-367-2024); James N Kirby Foundation; BF Foundation; Cure My Brain

Abstract

The promise of urinary extracellular vesicles (uEVs) in biomarker discovery is emerging. However, the characteristics and compositions of different uEV sub-populations across normal physiological and pathological states require rigorous explication. We recently reported proteomic signatures of small (s)-uEVs (<200 nm membranous nanoparticles) and described putative biomarkers corresponding to the diagnosis, tumour burden and recurrence of the lethal adult primary brain tumour, glioblastoma. Here, we comprehensively characterise uEV populations with significantly different mean and mode particle sizes obtained by differential centrifugation at $100,000 \times g$ (100K-uEVs; smaller) and $17,000 \times g$ (17K-uEVs; larger) using Fourier-transform infrared spectroscopy and quantitative data-independent acquisition mass spectrometry. We show distinct differences in protein and lipid content, prominent protein secondary structures, and proteome distributions between uEV populations that can distinguish glioblastoma patients from healthy controls and correspond to clinically relevant tumour changes (i.e., recurrence and treatment resistance). Among the key findings is a putative seven-protein biomarker panel associated with 17K-uEVs that could distinguish all glioblastoma patients from healthy controls and accurately classify 98.2% of glioblastoma samples. These novel, significant findings demonstrate that both uEV populations offer individual and combined biomarker potential. Further research is warranted to elucidate the complete diagnostic, prognostic, and predictive capabilities of often-neglected 17K-uEV populations.

KEYWORDS

Urinary extracellular vesicles, biomarkers, glioblastoma, liquid biopsy, proteomics, spectroscopy

1 | INTRODUCTION

Glioblastoma *IDH*-wildtype CNS WHO grade 4 (GBM) is the most common adult primary malignant brain tumour. Newly diagnosed patients are managed proactively, with a standard protocol of maximal surgical resection followed by radiotherapy with concurrent and adjuvant temozolomide chemotherapy. However, residual GBM tumour cells persist within the brain parenchyma

This is an open access article under the terms of the [Creative Commons Attribution-NonCommercial-NoDerivs License](https://creativecommons.org/licenses/by-nc-nd/4.0/), which permits use and distribution in any medium, provided the original work is properly cited, the use is non-commercial and no modifications or adaptations are made.

© 2024 The Author(s). *Journal of Extracellular Biology* published by Wiley Periodicals LLC on behalf of International Society for Extracellular Vesicles.

post-therapy, which leads to inevitable relapse with treatment-resistant GBM recurrence (Davis, 2016). There are limited treatment options for these highly heterogeneous and diffusely invasive tumours, particularly in the recurrent setting, and patients encounter a myriad of clinical challenges that contribute to the dismal 14-month median overall survival (Davis, 2016).

Radiological monitoring is the mainstay approach for assessing treatment response and recurrence in GBM patients. However, in approximately 30% of GBM patients undergoing standard treatment, neuroimaging cannot reliably distinguish tumour progression from radiological artefacts caused by treatment effects on the brain (i.e., pseudo progression and radiation necrosis), despite adjunctive modalities such as PET imaging and updated treatment response criteria such as RANO 2.0 (Abbasi et al., 2018; Zikou et al., 2018). In such cases, a definitive diagnosis is only possible through pathological assessment of biopsied tissues obtained via neurosurgical intervention, a clearly impractical and risky approach for routine tumour monitoring. Small biopsy specimens are also prone to sampling bias, an issue exacerbated by the intratumoural heterogeneity of GBM, meaning that the extent of a GBM recurrence can be difficult to determine (Sottoriva et al., 2013). Together, these factors hamper accurate early detection of GBM tumour recurrences and delays effective, timely clinical management that would otherwise improve patient outcomes.

In the search for a minimally invasive approach to accurately diagnose and monitor GBM tumours, extracellular vesicles (EVs; small membranous nanoparticles) have shown enormous potential as valuable biomarker reservoirs for liquid biopsy development. The field of EV research is rapidly evolving, and many EV subtypes have been described in the literature over the last decade (Di Vizio et al., 2012; Ma et al., 2015; Melentijevic et al., 2017; Vagner et al., 2018); the most investigated subtypes to date, within the 30–1000 nm size range, encompass three main classes of secreted vesicles: endosome-derived ‘exosomes’, plasma membrane-derived ‘microparticles’ and ‘ectosomes’, and apoptotic cell-derived apoptotic bodies (Akers et al., 2013; Pavlyukov et al., 2018). While there is currently no standardised classification system or universal molecular markers for the different EV subtypes, researchers are encouraged to meet the minimal information for EV studies reached by international consensus, and operational terms are recommended to describe the physical (i.e., size and density), biochemical (e.g., surface protein and lipid composition) and cell-of-origin properties/cellular processes of the EV populations studied (Théry et al., 2018; Welsh et al., 2024).

EVs released by GBM cells contain selectively packaged tumour molecules, including proteins, lipids, DNA, RNA and glycans (Del Bene et al., 2022; Quezada et al., 2018) that are protected from degradation by a lipid bilayer. They can also traverse physiological membranes (i.e., the blood-brain barrier) into the circulation (Bao et al., 2021; Xavier et al., 2020), where they are stable and can be readily captured. Indeed, GBM-released EVs are critical mediators of intercellular communication in the tumour microenvironment, exerting functional influence on recipient cells to promote tumour heterogeneity, invasive spread, chemoresistance, and immune evasion (Quezada et al., 2018). Thus, resolving the complex molecular cargo of EVs in the periphery can be used to detect dynamic GBM tumour changes for real-time patient monitoring (Ebrahimkhani et al., 2018; Hallal, Azimi et al., 2020; Hallal, Ebrahim Khani et al., 2020; Hallal et al., 2024). In the circulation, EVs are remarkably diverse in size, morphology, cargo, and origin, with EV populations arising from all cell types in the body (Welsh et al., 2024). Despite this diversity, we and others have explored EVs for GBM biomarkers in clinical biofluids (Ebrahimkhani et al., 2018; Hallal, Azimi et al., 2020; Hallal, Ebrahimkhani et al., 2019; Hallal, Russell et al., 2019; Hallal, Ebrahim Khani et al., 2020) and identified robust GBM biomarker signatures in EVs captured from neurosurgical aspirates (Hallal, Russell et al., 2019; Hallal, Ebrahim Khani et al., 2020), cerebrospinal fluid (Akers et al., 2013; Street et al., 2012), peripheral blood (Hallal, Azimi et al., 2020; Hallal, Ebrahim Khani et al., 2020) and most recently, the urine (Hallal et al., 2024). EV-associated biomarkers have shown promise for diagnosing diffuse glioma tumour subtypes and detecting changes associated with increased tumour aggression (Hallal, Azimi et al., 2020; Ebrahimkhani et al., 2018). In a recent feasibility study, we recovered urinary EVs (uEVs) from GBM patients before and after primary tumour resections and at confirmed tumour recurrences and identified robust protein signatures within small uEVs (<200 nm) corresponding to GBM tumour burden and recurrence (Hallal et al., 2024).

The urine is recognised as a rich, dynamic and heterogeneous source of EV populations, originating from various parts of the urogenital tract, including the kidney, bladder, prostate and uterovaginal tract, as well as from resident immune cells, bacteria and yeast (Erdrügger et al., 2021). The clinical relevance of capturing uEVs for detecting genitourinary disease biomarkers is well established (Abbastabar et al., 2020; Cricri et al., 2021; Erdrügger & Le, 2016; Erdrügger et al., 2021; Karpman et al., 2017; Sonoda et al., 2019). Emerging reports, however, suggest that urine is also a valuable source of EV-associated biomarkers for conditions extending beyond the urogenital tract (Fraser et al., 2016; Street et al., 2012; Sun et al., 2019; Wang et al., 2019). Several studies show striking enrichments of EV-cargo biomarkers in the urine associated with neurological disorders, including Parkinson’s, Alzheimer’s and Huntington’s disease (Fraser et al., 2016; Street et al., 2012; Sun et al., 2019; Wang et al., 2019), as well as in oncology, including lung (Li et al., 2011) and breast cancers (Hirschfeld et al., 2020; Sun et al., 2019). Theoretically, urine is an ideal biofluid for routine non-invasive tumour assessments as large volumes can be regularly and non-invasively sampled to capture highly stable uEV particles (Erdrügger et al., 2021).

As the urinary system is a potential route of EV clearance from the body, EVs from the circulation must pass through the kidney’s glomerular filtration barrier to enter the urine. It is possible that smaller EVs simply traverse the 50–100 nm fenestrations of the capillary endothelium (Ndisang, 2018), however, the pore sizes of the slit diaphragm (approximately 6–8 nm in healthy conditions) likely restrict the direct passage of EVs into the urine (Erdrügger et al., 2021; Patrakka et al., 2002). Pathological conditions, such as minimal change nephrotic syndrome (Patrikka et al., 2002) and diabetes (Ndisang, 2018), are proposed to enlarge

TABLE 1 Overview of the urinary-EV experimental cohorts.

Experimental Cohort	Description	Sample <i>n</i>	Gender Female:Male	Mean age (years) \pm SD
GBM PreOP	Pre-operative primary GBM	13	4 F:9 M	62.1 \pm 14.1
GBM PostOP	Post-operative primary GBM	7	4 F:3 M	62.9 \pm 13.6
GBM REC	Pre-operative GBM recurrence	6	4 F:2 M	60.3 \pm 19.3
HC	Healthy control	14	7 F:7 M	69.4 \pm 3.7

the slit diaphragm's pore sizes to 70 nm, potentially enhancing the passage of smaller EVs from the circulation into the urine (Erdbrügger et al., 2021; Patrakka et al., 2002). Alternatively, EVs may enter the urine via transcytosis, a process where circulating EVs and non-vesicular proteins are endocytosed by renal tubular cells or podocytes, then packaged into EVs and secreted into the urinary space. The transcytosis route is supported by observations of circulatory albumin associated with uEVs (Kerjaschki et al., 1989; Londono & Bendayan, 2005; Musante et al., 2020), and the relative under-representation of urogenital tract resident proteins in the protein cargo of uEVs (Wang et al., 2019). Nonetheless, the exact mechanisms by which small and large sized EVs pass from the circulation into the urine remain unclear (Erdbrügger et al., 2021).

We identified only one investigation that explored the molecular profiles of small (s-) and large (l-) uEVs in genitourinary disorders (Bruschi et al., 2019), and we note the absence of any study examining different uEV subpopulations in oncology. Previously, we demonstrated the feasibility of using protein biomarkers associated with smaller (<300 nm) uEV populations isolated at 100,000 \times *g* (100K-uEVs) for a GBM 'liquid gold' biopsy (Hallal et al., 2024). Here, we extend this work by investigating the compositional variances between 100K-uEVs with overall larger uEVs populations pelleted at the interim differential centrifugation method step (17,000 \times *g*; 17K-uEVs). We evaluated the biomolecular variations of the two uEV populations in GBM and healthy controls using Fourier-transform infrared spectroscopy (FT-IR) and data-independent acquisition mass spectrometry (DIA-MS) (Gillet et al., 2012). Additionally, we investigate the proteomes of 17K-uEVs and test their feasibility as potential biomarkers for GBM. Our findings reveal significant differences in uEV lipid composition and proteome distributions between 100K-uEVs and 17K-uEVs in GBM patients relative to healthy controls, and at key GBM clinical stages. Thus, we argue that 17K-uEVs represent an untapped EV compartment rich with biomarker potential.

2 | MATERIALS AND METHODS

2.1 | Cohort information and urine collection

Urine specimens were collected from catheterised GBM patients and stored at -80°C by the Sydney Brain Tumour Bank (SLHD HREC X19-0010). This biomarker discovery study was performed under the approved human ethics protocol, USYD HREC 2019/705. Urine (20–100 mL) was collected from participants diagnosed with glioblastoma, IDH-wildtype, CNS WHO2021 Grade 4 (Classification of Tumours Editorial Board, 2023), at three distinct clinical time points, that is, before (PreOP; *n* = 9) and after surgical removal of primary tumours (PostOP; *n* = 7), and prior to the surgical removal of a GBM recurrence (REC; *n* = 6). All PreOP urine specimens were collected immediately prior to surgery and PostOP samples were collected the day following a gross total resection (average 18.3 h post-surgery). GBM urine samples were compared to urine from age- and gender-matched healthy controls, collected as mid-stream, first morning pass urine specimens (HC; *n* = 13). A summary of experimental cohorts is provided in Table 1; refer to Table S1 for additional demographic and clinical details, as well as GBM patient blood and urine biochemistry (includes creatinine and protein concentration).

2.2 | Isolation and characterisation of urinary extracellular vesicles

To isolate the uEV populations, thawed urine samples (20–100 mL) were subjected to a differential ultracentrifugation protocol, described before (Hallal et al., 2024). Briefly, an initial 3000 \times *g* centrifugation step was used to deplete cell debris and larger particles, followed by 17,000 \times *g* for 30 min at 4°C to pellet 17K-uEVs; the supernatant was kept for further processing. The 3000 \times *g* pellet was treated with a reducing mixture at a final concentration of 5 mM (tris(2-carboxyethyl)phosphine hydrochloride) TCEP-HCl/50 mM Tris-HCl/25 mM sucrose (15 min at RT) to release uEVs entrapped within lattice-like uromodulin polymer networks that form during low-speed centrifugations (Fernández-Llama et al., 2010; Welsh et al., 2024). The reducing mixture was then diluted seven-times with 4 mM TCEP-HCl/10 mM Tris/HCl, followed by a 17,000 \times *g* (30 min, 4°C) spin. The initial and treated 17,000 \times *g* supernatants were then combined and ultracentrifuged (100,000 \times *g*, 2 h, 4°C in 38 \times 102 mm Beckman Coulter polycarbonate bottles; fixed angle rotor F-37L-8 8 \times 100 mL, THERMO WX 100; 100K-uEVs). The workflow

to isolate the 17K-uEVs and 100K-uEVs is outlined in Figure 1a. A portion of 100K-uEV specimens used in this study overlap with those used in our pilot study on s-uEVs for a ‘liquid gold’ GBM biopsy (Hallal et al., 2024); these overlapping samples are marked with an asterisk in Tables S2–4.

EV populations were characterised using orthogonal methods according to the latest guidelines of the International Society for Extracellular Vesicles on the Minimal Information Required for Studies of Extracellular Vesicles (MISEV2023) (Welsh et al., 2024). EV size distributions and concentrations were measured by nanoparticle tracking analysis software (NTA, version 3.0) using the NanoSight LM10-HS (NanoSight Ltd., Amesbury, UK), configured with a 532 nm laser and a digital camera (CMOS Trigger Camera). EVs were diluted in filtered PBS (viscosity 1.09 cP) to ensure that 20–100 particles were detected in the field of view in the standard CCD camera of the microscope. The NTA video recordings (60 s) were captured in triplicate at 25 frames/s with default minimal expected particle size, minimum track length, and blur setting, a camera level of 11 and a detection threshold of 5. The temperature of the laser unit was controlled at 25°C. NTA software measured the size distribution (ranging from 10 to 1000 nm), concentration (particles/ml), mean (nm) and modal (nm) sizes of the nanoparticle populations by simultaneously tracking Brownian motion and light scatter of individual laser-illuminated particles and calculating their diameter using statistical methods (Dragovic et al., 2011). The 17K-uEV and 100K-uEV samples were also imaged by cryogenic-transmission electron microscopy (cryo-TEM), as previously described at Sydney Microscopy and Microanalysis, University of Sydney (Mastronarde, 2005). Briefly, the 100K-uEV and 17K-uEV samples were applied to copper 300-mesh lacey carbon grids and plunged frozen into ethane using a Vitrobot IV (ThermoFisher). The grids were imaged using SerialEM (Mastronarde) on a ThermoFisher Glacios (operated at 200 kV) equipped with a Falcon III camera (ThermoFisher) at 22,000X or 45,000X magnification. Image scale bars were determined in ImageJ 1.53K software. Lastly, liquid chromatography-tandem mass spectrometry (LC-MS/MS) was used to assess the purity of EVs from common contaminants, the intracellular origin of the EVs, and to identify the presence of EV features through canonical EV markers and the presence of the top 100 EV-marker proteins as curated in Vesiclepedia, a compendium of EV-associated molecules (the LC-MS/MS method is detailed below in Section 2.4).

2.3 | Fourier-transform infrared spectroscopy of urinary-EVs: data capture, analysis and interpretation

Paired 100K-uEV and 17K-uEV pellets from the urine of four healthy individuals (50 mL urine; uEV pellets resuspended in 100 μ L de-ionised H₂O) and four pre-operative GBM patients (10–25 mL; uEV pellets resuspended in 100 μ L PBS) were characterised by Fourier-transform infrared spectroscopy (FT-IR). FT-IR is a non-invasive, label-free, high-throughput method that utilises the absorption of IR radiation to determine the vibrational modes of molecular functional groups. When applied to biological samples, FT-IR reveals valuable information related to sample composition, structure and molecular interactions (Ami et al., 2013; Amir et al., 2013). Each uEV sample (2–4 μ L) was evenly spread onto a 96-well silicon plate and dried in ambient air for 3 h prior to data collection. Infrared spectra were collected for the paired 100K-uEV and 17K-uEV specimens using a Bruker Tensor 27 FT-IR spectrometer coupled to a high-throughput sampling extension module (HTS-XT, Bruker Optics, Ettlingen, Germany). The spectrometer is equipped with a KBr beam splitter and deuterated L-alanine doped triglycine sulphate (DLATGS) detector, and the humidity was controlled via two desiccant cartridges (one located within the spectrometer and the other within the HTS-XT). Spectra were collected over the region of 400–4000 cm^{-1} at a spectral resolution better than 0.9 cm^{-1} with the co-addition of 256 scans. Each sample was run in triplicate to ensure measurement reproducibility. A background reading was collected from an empty well before each sample acquisition to minimise spectral variations caused by background noise. The FT-IR spectral data were subject to atmospheric correction for CO₂, H₂O and aqueous solutions, followed by vector normalisation and baseline correction (rubberband method) using OPUS 8.7.3.1 (Bruker Optics) software. The corrected, triplicate FT-IR spectra for 100K-uEV and 17K-uEV specimens were further analysed and visualised with Orange Data Mining 3.35 software.

Spectral assessments of HC uEVs were performed for FT-IR peaks between 700–3800 cm^{-1} . FT-IR spectral peak assessments for GBM uEVs were restricted to 1300–3800 cm^{-1} peaks due to the presence of PBS in the GBM uEV preparations which contribute convoluted signals between 900 and 1300 cm^{-1} from phosphate vibrations (Movasaghi et al., 2008). To visualise the multidimensional 100K-uEV and 17K-uEV FT-IR spectra, we used t-distributed stochastic neighbour embedding (t-SNE), a dimensionality reduction algorithm, and principal component analysis (PCA). The t-SNE was performed on 50 principal components and optimised with a measure of perplexity value of 30. Spectral data for 100K-uEV and 17K-uEV samples were averaged, and the most prominent peaks were identified and selected for further assessment.

For FT-IR data interpretation, we drew on observations reported in the literature for FT-IR peak profiles of nucleic acids, carbohydrates, phospholipids, proteins, peptides, lipids and fatty acids; corresponding FT-IR spectra are summarised in Figure S4. To decipher overlapping peaks associated with protein secondary structure, the second derivative FT-IR spectra (which allows increased resolution) were plotted using averaged 100K-uEV and 17K-uEV signals with a Savitzky-Golay filter: window, 5; polynomial order, 3; derivative, 2. The relative second derivative peak heights were compared for β -pleated sheets (1615–1638 cm^{-1}) to β -turns (1658–1688 cm^{-1}). The relative proportions of lipid-to-protein content were estimated for 100K-uEVs and 17K-uEVs using a pseudo-Voigt peak fitting model, a Voigt approximation from a weighted sum of Gaussian and Lorentzian functions

(Bösel et al., 2023). The sum of the area under the peaks associated with CH_2/CH_3 stretching ($2700\text{--}3000\text{ cm}^{-1}$) and amide I region ($1580\text{--}1720\text{ cm}^{-1}$) was used to estimate the average lipid and protein concentrations (a.u.) (Mihály et al., 2017).

2.4 | EV proteome preparation for data-independent acquisition mass spectrometry

uEV proteomes were extracted and prepared for LC-MS/MS analysis using established methods (Hallal et al., 2024). Briefly, the EV pellets were resuspended in 0.2% (w/v) Rapigest SFTM (Waters, Milford, MA, USA) in 0.05 mol/L triethylammonium bicarbonate (TEAB), incubated at 95°C for 5 min and sonicated twice with a step-tip probe at 30% intensity for 20 s to aid EV lysis and protein resuspension. The protein content of the uEV pellets was estimated using the Qubit[®] Protein Assay Kit (Invitrogen, Carlsbad, CA, USA) and 25–50 μg EV protein aliquots were digested by sequencing-grade trypsin (Promega, Madison, WI) in a 1:30 (w/w) trypsin: protein ratio and desalted by solid-phase extraction using lcc HLB cartridges (Waters, MA, USA).

Desalted peptides (300 ng) were analysed using a Q-ExactiveTM HFX hybrid quadrupole-orbitrap mass spectrometer (Thermo Scientific, MA, USA). Peptide mixtures (0.1 $\mu\text{g}/\mu\text{L}$) resuspended in 3% (v/v) ACN/0.1% (v/v) FA were separated by nano-LC using an Ultimate 3000 UHPLC and autosampler system (Dionex, Amsterdam, Netherlands). Reverse-phase mobile buffers were composed of A: 0.1% (v/v) FA (Thermo Scientific, MA, US, Cat No. 34851-4), and B: 80% (v/v) ACN (Thermo OPTIMA LC-MS grade, Cat No. 34851-4)/0.1% FA. Peptides were eluted using a linear gradient of 5% B to 42% B across 140 min with a constant flow rate of 250 nL min^{-1} . High voltage (2000 V) was applied to a low-volume tee (Valco, Houston, TX, USA), and the column tip was positioned approximately 0.5 cm from the heated capillary ($T = 275^\circ\text{C}$) of the MS. Positive ions were generated by electrospray, and the Orbitrap was operated in data-independent acquisition (DIA) mode. A total of 20 variably sized windows (including 1.0 Da window overlap) were generated, covering a precursor mass range of 350–1650 m/z. The m/z ratios selected for MS/MS were dynamically excluded for 20 s. An LC-MS/MS standard consisting of 30 fmol pre-digested BSA (GeneSearch, QLD, Australia, Cat No. P8108S, 500 pmol) ensured the instrument was performing optimally. The LC-MS/MS standard injection was repeated throughout the analysis along with one patient sample to ensure that the technical reliability and sensitivity of the instrument were maintained.

2.5 | Analysis of DIA-MS data

A comprehensive GBM spectral library previously generated from primary patient-derived GBM cells, GBM-EVs enriched from surgical fluids and GBM tumour tissues (Hallal, Azimi et al., 2020) was used for targeted DIA-MS data extraction of uEV proteomes. The library contained spectral data for 8651 protein groups and 186,037 precursors. The DIA-MS data was aligned and searched against the spectral library using data independent neural network (DIA-NNTM) with the following parameters: trypsin, two missed cleavages; maximum number of variable modifications, 2; variable peptide modifications, M excision, carbamidomethylation and oxidation; peptide length range, 7–30; precursor m/z range, 300–1800; fragment ion m/z range, 100–2000; precursor false discovery rate, 1%; quantification strategy, robust LC (high accuracy). The mass accuracy was optimised by DIA-NN, and scan windows were inferred separately for each data sample.

After removing low-confidence identifications and interfering precursors, DIA-NN allowed a MaxLFQ-based protein quantification of the proteins identified at a 1% false discovery rate (FDR). The MaxLFQ abundance values for identified proteins were output into quantities matrices. The repeatability and reproducibility of the DIA-MS approach were assessed by correlating the abundances of replicate MS injections of the same uEV sample (UH10 100K-uEV, Int Ctrl) captured at four time points during the data acquisition (Int Ctrl 1, 2, 3, and 4). Int Ctrl 1 and 2 were analysed during the DIA-MS acquisition of 100K-uEV samples ($n = 35$), and Int Ctrl 3 and 4 were analysed during the subsequent acquisition of 17K-uEV ($n = 35$) peptide samples. The goodness-of-fit measure for linear regression (coefficient of determination, R^2) found high reproducibility and repeatability of the replicate injections; $R^2 > 0.9585$ and stable protein identifications (Figure S1).

2.6 | DIA-MS data filtering, normalisation, statistics, and visualisation

We adopted a global absolute normalisation method, conducting DIA-MS analyses on equal amounts of total uEV proteins (300 ng). The DIA-MS uEV data was filtered, processed and normalised with Perseus 1.6.5.0 (Tyanova et al., 2016). Protein abundance levels were processed by a log₂ transformation, followed by imputation of missing values from the normal distribution and quantile normalisation to adjust for differences in sample size and measurement bias. Proteins identified in 100% of samples were selected for comparative analysis between 100K-uEVs and 17K-uEVs. Comparative analyses between 17K-uEV cohorts were performed on proteins present in at least 80% of samples in each cohort (HC, GBM PreOP, GBM PostOP and GBM REC). The proteomes of each cohort were annotated to Vesiclepedia, and sites of expression and cellular components were characterised using FunRich 3.1.3 (Pathan et al., 2015).

Normalised data were used to calculate fold changes, and Student's *t*-tests (assuming equal variance) were performed to determine the statistical difference between sample cohorts. Differentially abundant proteins were visualised with volcano plots using OriginPro. Orange Data Mining 3.35 software was used to generate Euclidean distance maps and PCA plots to observe the clustering patterns of sample groups. Significant 17K-uEV proteins corresponding to a GBM diagnosis (PreOP GBM vs. HC; p -value < 0.05) were assessed using a logistic regression model with L2 Regularisation ($C = 1$) in a supervised learning approach. The model ranked the proteins by importance for classifying GBM based on the magnitude of their coefficients (β). A step-wise selection method was applied to the top-ranking proteins to determine protein combinations that had the best collective performance under a L2-regularised logistic regression model ($C = 1$). A multivariate logistic regression model was trained and tested 100 times with a data split of 75%-training and 25%-testing. Performance metrics included average Area Under the Curve (AUC), classification accuracy (CA), F1 score, precision, recall, specificity and log loss metrics. Using GraphPad Prism 10, the best-performing proteins were individually assessed with a receiver operating characteristic (ROC) curve, and the AUC summarised their overall performance in terms of sensitivity and specificity. Box plots were created using GraphPad Prism 10.

2.7 | Functional annotations of identified proteins

Pathway analysis was performed using Ingenuity® software (Ingenuity Systems, USA; <http://analysis.ingenuity.com>) to assess functional associations (biological and canonical pathways) of differentially abundant proteins ($p \leq 0.05$) by performing core expression analyses using default criteria. The Database for Annotation, Visualisation and Integrated Discovery (DAVID) was used to generate functional annotation charts for protein lists that are exclusive to 100K-uEVs and 17K-uEVs, and for protein lists with significant differential abundance between 100K-uEVs and 17K-uEVs, using default annotation settings. Listed annotations had a fold-enrichment > 2 and FDR < 0.01.

2.8 | Data availability

The GBM spectral library is available in PeptideAtlas with the identifier PASS01487. The MaxLFQ data generated by DIA-NN used for this study is provided in Table S2. The RAW LC-MS/MS proteomics data has been deposited to the ProteomeXchange Consortium via the PRIDE partner repository with the dataset identifier PXD051553 (Perez-Riverol et al., 2022).

3 | RESULTS

3.1 | Characterisation of small and large urinary-EV populations

uEV populations were isolated from urine by differential ultracentrifugation; 17K-uEVs were recovered by $17,000 \times g$ centrifugation, and 100K-uEVs were pelleted by $100,000 \times g$ ultracentrifugation (Figure 1a). Cryo-TEM images for 100K-uEVs and 17K-uEVs reveal rich polydisperse vesicular structures devoid of surrounding lattice-like networks, indicating no apparent contamination with uromodulin polymers. The 100K-uEVs are comprised of vesicular populations, ranging from 50 to 200 nm, that have well-defined round-circular morphologies with single, double, or quadruple membranes (Figure 1b-1). The 17K-uEV particles exhibited a greater diversity in size and morphology; 17K-uEV diameters ranged from 70 to 600 nm and showed rounded and complex ellipsoid-shaped vesicles with both singular and multiple membranes (Figure 1b-2). NTA corroborates the micrograph observations, which show that 17K-uEVs are comprised of heterogeneous particle populations with larger size distributions (80–600 nm; $n = 9$) relative to 100K-uEVs (80–400 nm; $n = 9$). Specifically, 100K-uEV fractions include a major population of 117.5 nm-sized particles and a minor population of 282.5 nm-sized particles. In comparison, the most prominent 17K-uEV population is measured at 147.5 nm with smaller populations at 102, 122.5, 197.5, 272.5 and 377.5 nm (Figure 1c). Overall, 17K-uEVs had greater mean and modal sizes (mean, 215.1 ± 3.3 nm; mode, 151.0 ± 18.9 nm) than 100K-uEVs (mean, 160.2 ± 3.3 nm; mode, 116.1 ± 7.6 nm, Figure S2A).

Paired 100K-uEV and 17K-uEV samples isolated from 35 urine specimens (GBM and HC; Table S1) were characterised using our established DIA-MS workflow (Hallal et al., 2024). Overall, a total of 6834 proteins were confidently identified across all 100K-uEV and 17K-uEV specimens (q -value < 0.01; Table S2). A total of 2294 and 928 proteins were identified in 100K-uEVs and 17K-uEVs, respectively, in at least 80% of urine specimens (28/35) and were well represented by the top-100 EV proteins, as reported by Vesiclepedia [100K-uEV (91/100); 17K-uEV (83/100); Table S3]. More stringently, 683 and 205 proteins were confidently identified in all 100K-uEV and 17K-uEV samples, respectively, with 199 proteins sequenced in both uEV populations (Figure 1d, Tables S3 and S4). Functional enrichment analysis showed that the proteomes of both uEV fractions are largely annotated to exosomes, as well as other membrane compartments of the cell (Figure 1e-1), and proteins are expressed in relevant sites, including the brain

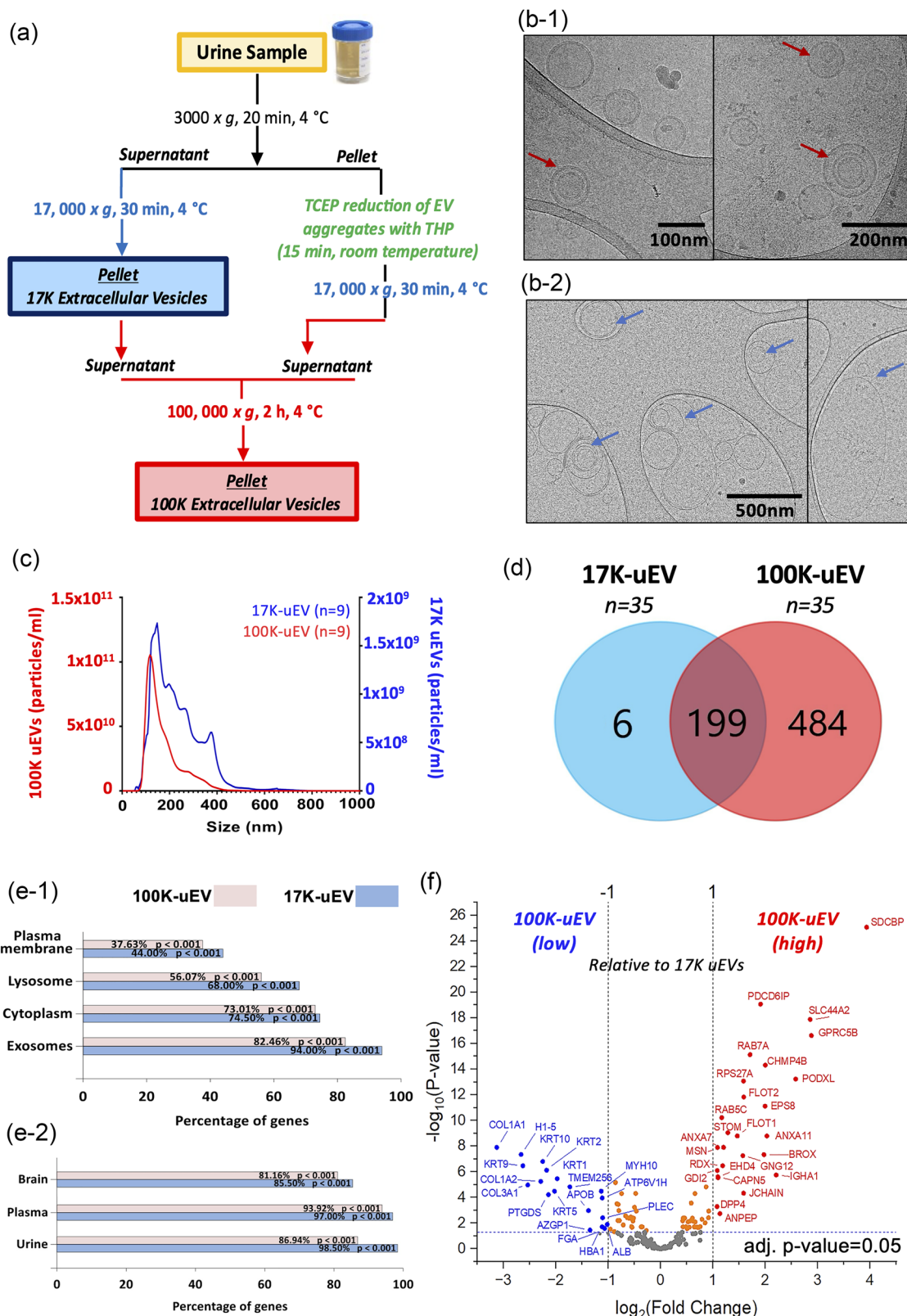


FIGURE 1 Characterisation of 100K and 17K urinary extracellular vesicle pellets. (a) The differential centrifugation workflow included the isolation of urinary-EVs at 17,000 × g (17K-uEVs) and at 100,000 × g (100K-uEV) from urine. Cryo-transmission electron microscopy imaged (b-1) 100K-uEVs at 45,000X magnification and (b-2) 17K-uEVs at 22,000X magnification. (c) The average particle size distribution of paired 100K-uEVs (red) and 17K-uEVs (blue) populations determined by nanoparticle tracking analysis (NTA, n = 9). (d) A data-independent mass spectrometry (DIA-MS) analysis of paired 100K-uEVs and 17K-uEVs (n = 35) identified a total of 683 and 205 proteins, respectively, with a substantial overlap of 199 protein species. The uEV protein profiles had significant functional annotations to (e-1) membrane compartments of the cell and (e-2) sites of expression including the brain, plasma and urine. (f) A volcano plot shows proteins with significant differential abundance between 100K-uEVs and 17K-uEVs; red proteins have higher levels (FC > 2, adjusted p-value < 0.05) and blue proteins have lower levels (FC < 2, adjusted p-value < 0.05) in 100K-uEVs relative to 17K-uEVs.

(81.2%–85.5%), plasma (93.2%–97.0%) and urine (86.9%–98.5%). Interestingly, higher proportions of the 17K-uEV proteome were annotated to the brain, plasma, and urinary compartments relative to 100K-uEVs (Figure 1e–2).

Six proteins (including ATP6AP1, KRT18, LAIR1, SERPINA3, VASN and KPNB1) were exclusively identified in all 17K-uEV samples, whereas 484 proteins were specific to the 100K-uEV fraction (Figure 1d, Table S4). The 484 proteins restricted to 100K-uEVs include canonical EV proteins (CD63, CD81, CD9, TSG101, ITGB1, FLOT1, LGALS3BP, RAC1, YWHAG, VCP), different chaperone classes (i.e., TRiC subunits—TCP1, CCT2, CCT3, CCT4, CCT5, CC6A, CCT8, and heat shock proteins—HSP90B1, HSPA12A and HSPA9), members of the Ras oncogene family (RAB10, RAB14, RAB1B, RAB21, RAB23, RAB2A, RAB35, RAB5A, RAB8A, RAB8B) and Rho family proteins (RHOA, RHOB, RHOC, RHOG). Using DAVID, the 100K-uEV restricted proteins were annotated to functions frequently observed in EV studies, including membrane trafficking (fold-enrichment = 3.0, p -value = 1.2×10^{-16}), signalling by Rho GTPases (fold = 2.6, p -value = 3.9×10^{-13}), endosomal sorting complex required for transport (ESCRT; fold = 11.3, p -value = 4.7×10^{-10}), signal transduction (fold = 1.4, p -value = 2.5×10^{-6}), chaperonin-mediated protein folding (fold = 3.4, p -value = 1.4×10^{-3}), and integrin signalling (fold = 5.4, p -value = 4.6×10^{-6}).

As above, a substantial overlap of 199 proteins was detected in all paired 100K-uEVs and 17K-uEVs samples ($n = 35$; Figure 1d, Table S4). Proteins common to 17K-uEVs and 100K-uEVs were significantly annotated to the extracellular exosome (fold = 8.7, p -value = 4.1×10^{-164}), blood microparticle (fold = 25.4, p -value = 3.6×10^{-39}), extracellular space (fold = 4.3, p -value = 6.4×10^{-32}), focal adhesion (fold = 10.6, p -value = 2.8×10^{-31}), vesicle-mediated transport (fold = 3.6, p -value = 4.1×10^{-12}), calcium-dependent protein binding (fold = 14.3, p -value = 4.12×10^{-12}) and cell surface (fold = 4.1, p -value = 4.2×10^{-9}). Interestingly, the abundance levels of these shared proteins were sufficient to separate 100K-uEV and 17K-uEV samples on a PCA plot (Figure S2B). Of the overlapping 199 proteins, 45 were significantly differentially abundant between the uEV populations (absolute fold change, $|FC| \geq 2$; Benjamini-Hochberg adjusted p -value < 0.05 ; Figure 1f). Proteins with higher levels in 100K-uEVs include those commonly associated with EVs and EV biogenesis, that is, ANXA7, ANXA11, BROX, CHMP4B, EHD4, FLOT1, GNG12, MSN, GDI2, PDCD6IP, RAB5C, RAB7A, SDCBP, SLC44A2, as well as proteins involved in glomerular filtration, such as IGHA1, JCHAIN and PODXL. Proteins with significantly higher abundances in the 17K-uEVs include serum proteins, that is, ALB, APOB, AZGP1, FGA, HBA1, as well as collagens (COL1A1, COL1A2, COL3A1), keratins (KRT1, KRT2, KRT5, KRT9, KRT10) and transmembrane proteins (TMEM256 and ATP6V1H; Figure 1f). A Euclidean distance map based on the 45 significant differentially abundant proteins highlights the distinct protein profiles of 100K-uEV from 17K-uEV populations (Figure S2C).

3.2 | The biochemical properties of 100K-uEVs and 17K-uEVs determined by Fourier transform infrared spectroscopy (FT-IR)

The overarching spectral properties of paired 100 and 17K-uEV samples isolated from HCs ($n = 4$) were evaluated between 700 and 3800 cm^{-1} in technical triplicate. The FT-IR absorbance spectra for each of the four uEV paired specimens are provided in Figure S3A; 14 prominent, distinguishable spectral peaks were observed for 100K-uEVs and 12 for 17K-uEVs (Figure 2a). A comparative summary of the 100K-uEV and 17K-uEV peaks are provided in Figure S4, and includes their wavenumber (cm^{-1}), corresponding functional group vibrations and key biological compounds. Although 100 and 17K uEVs display similar FT-IR absorbance peaks (785, 942, 1162, 1238, 1630, 1669, 3215, 3343 and 3437 cm^{-1}), inherent spectral differences between the pairs of uEV populations were observed (Figure 2a), as depicted by a t-SNE plot (Figure S3B). Within 780–1270 cm^{-1} regions, 100K populations have more prominent signals associated with symmetric (1076 cm^{-1}) and asymmetric (1238 cm^{-1}) phosphate (PO_2) stretching of nucleic acids and phospholipids compared to 17K-uEVs (Figure 2a, Figure S4). Peak differences are also present in regions associated with lipids/acyl chains (1458–1465 cm^{-1} and 2700–3000 cm^{-1}). Interestingly, while both 100K-uEVs and 17K-uEVs exhibit clear signals associated with methyl (CH_2/CH_3) bending (1458–1465 cm^{-1}) (Movasaghi et al., 2008), differences are observed in the region associated with methyl stretching (2700–3000 cm^{-1}) where peaks for symmetric CH_2 (2852 cm^{-1}), asymmetric CH_2 (2923 cm^{-1}) and asymmetric CH_3 (2957 cm^{-1}) stretching are present in 100K-uEVs but absent in 17K-uEVs (Figure 2a) (Movasaghi et al., 2008); this observation was noted with no coinciding peak shifts (3000–3100 cm^{-1}) in 17K-uEVs that usually occur with unsaturated lipid components (Christy & Egeberg, 2006; Derenne et al., 2013; Lewis & McElhaney, 2013).

Across the mid-IR range, the most noticeable spectral peaks appear in the amide I region (1600–1700 cm^{-1}), which is associated with proteins and peptides (Figure 2a). Here, the 100K-uEVs and 17K-uEVs share two vibrational peaks that are characteristic of protein secondary structures, including β -pleated sheets (1630 cm^{-1} peak) and β -turns (1669 cm^{-1}) (Naumann, 2001; Romanò et al., 2020). However, differences in the height and shape of these peaks suggest distinct protein structural confirmations between the two uEV populations (Figure 2a). Calculating the second derivative of the amide I peaks enhanced their resolution and allowed the comparison of their peak heights (Figure S3C). The β -pleated sheets to β -turn peak height ratios were 0.53 for 100K-uEVs and 3.67 for 17K-uEVs, indicating β -pleated sheet enrichment in 17K-uEV proteins and β -turn enrichment in 100K-uEV proteins (Table 2).

FT-IR spectral differences in the 3200–3600 cm^{-1} region reveal variations in carboxyl and amino groups between 100 and 17K-uEVs. Both populations exhibit carboxylic acid O–H stretching at 3215 cm^{-1} and primary amine stretches at 3343 cm^{-1} and

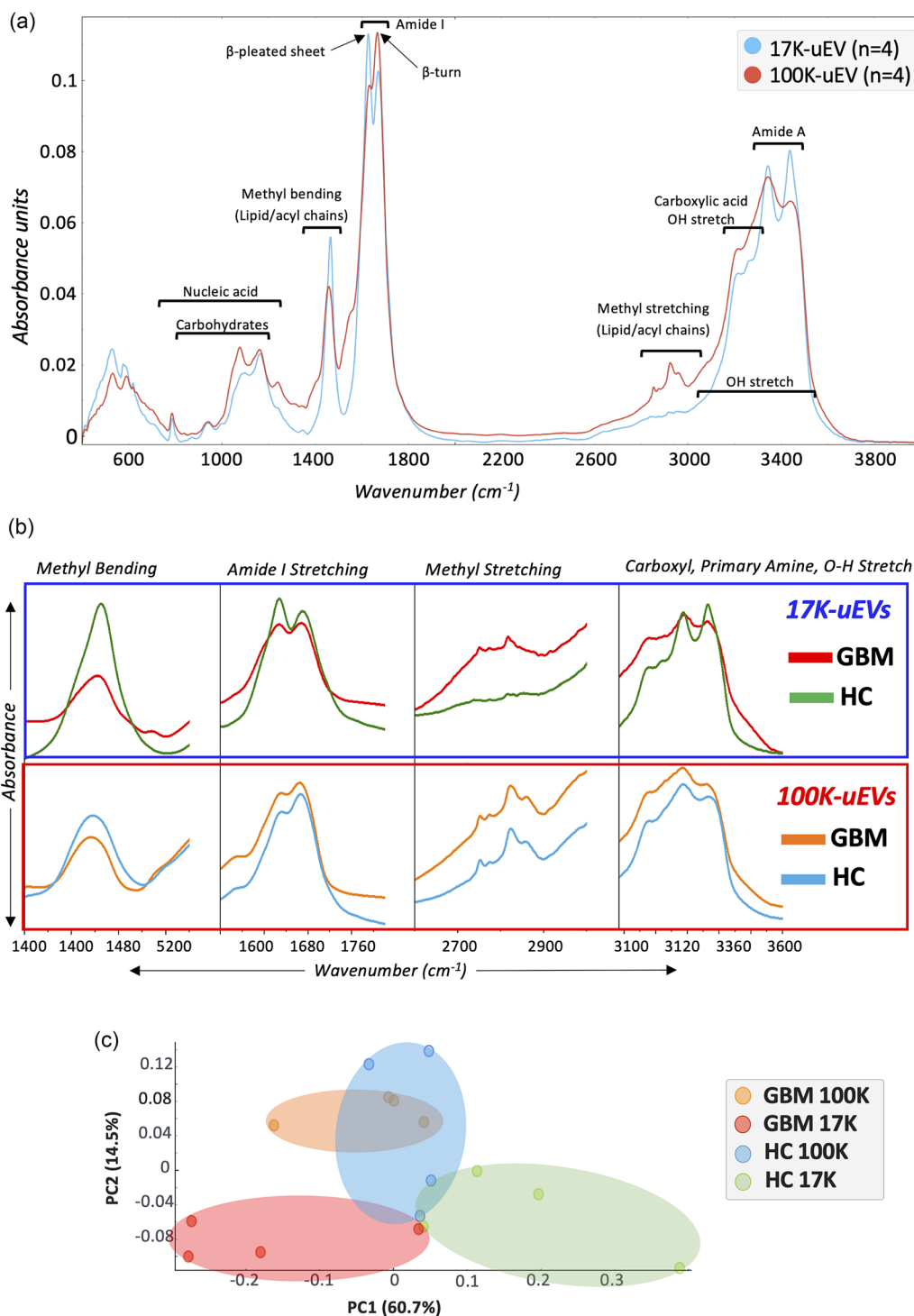


FIGURE 2 Evaluation of the Fourier Transform Infrared Spectroscopy (FT-IR) spectral differences between the 100K-uEVs and 17K-uEVs of glioblastoma (GBM) patients compared to healthy controls (HC). Paired 100K-uEV and 17K-uEV specimens isolated from the urine of four healthy individuals (urine-1, urine-2, urine-3, urine-4; Figure S3A) were analysed by FT-IR in triplicate within the mid-IR region (400–4000 cm^{-1}). (a) An overlay of the average FT-IR absorbance spectral profiles for uEVs isolated at 100K (red, $n = 4$) and 17K (blue, $n = 4$) shows 14 prominent peaks for 100K-uEVs and 12 prominent peaks for 17K. Spectral variances are observed between 100 and 17K uEVs for functional group vibrational modes that are typically associated with nucleic acids, carbohydrates, lipids/acyl chains, amide I, and amino acid side chains (carboxylic acids and Amide A). (b) Biochemical profiles of uEVs from GBM patients and HCs were qualitatively assessed in regions associated with methyl bending (1400–1530 cm^{-1}), amide I stretching (1520–1840 cm^{-1}), methyl stretching (2700–3100 cm^{-1}), and carboxyl/primary amine/OH stretches (3000–3800 cm^{-1}). The average FT-IR peak profiles for 17K-uEVs (upper blue panel) are shown for GBM ($n = 4$, red) and HC ($n = 4$, green) and average peak profiles for 100K-uEVs (bottom red panel) from GBM ($n = 4$, orange) and HC ($n = 4$, blue). (c) A Principal Component Analysis (PCA) based on the FT-IR absorbances corresponding to methyl bending, amide I stretching, methyl stretching and carboxyl/amide A/O-H stretching, illustrates the clustering patterns for paired 100K-uEV and 17K-uEV specimens from GBM ($n = 4$) and HC ($n = 4$).

TABLE 2 FT-IR spectral quantitative estimation of the relative proportions of protein secondary structures (β -pleated sheets and β -turns) and lipid-to-protein content in 100K-uEVs and 17K-uEVs.

Relative quantitation method	Biomolecular region	Healthy controls (HC)		Glioblastoma (GBM)	
		100K-uEVs	17K-uEVs	100K-uEVs	17K-uEVs
2nd derivative relative peak heights	β -sheets (1615–1638 cm^{-1})	−0.00013	−0.00100	−0.00025	−0.00021
	β -turns (1658–1688 cm^{-1})	−0.00024	−0.00027	−0.00029	−0.00018
	β-sheets: β-turn ratio	0.53	3.67	0.86	1.14
Sum area under the curve of peak fitting	Protein (amide I, 1600–1700 cm^{-1})	19.21	20.34	19.63	29.20
	Lipid (methyl stretching, 2700–3000 cm^{-1})	34.32	4.73	45.94	74.43
	Lipid:Protein ratio	1.79	0.23	2.34	2.55

3437 cm^{-1} . The 17K-uEVs have sharp primary amine peaks, indicating that the peaks are caused by distinct, well-defined primary amine functional groups. In contrast, the 100K-uEVs show broader peaks, suggesting more complex molecular interactions between the functional groups (Figure 2a). A pseudo-Voigt curve fitting method was used to estimate the protein and lipid compositions of the EV populations, and showed that 100K-uEVs contain 1.79-fold more lipids than proteins, whereas 17K-uEVs are 4.25-fold richer in proteins (Table 2).

3.3 | Biochemical compositional differences in uEV populations captured from GBM patients

We then analysed the biochemical differences between 100K-uEV and 17K-uEVs from GBM patients (PreOP samples) and HCs. GBM 100K-uEVs shared nine prominent peaks with HC 100K-uEV peaks (1457, 1631, 1665, 2850, 2923, 2963, 3215, 3342 and 3435 cm^{-1} ; Figure 2b). GBM 17K-uEVs shared eight prominent peaks with HC 17K-uEVs (1463, 1627, 1669, 2852, 2917, 3220, 3347 and 3435 cm^{-1}), with unique peaks at 2917 cm^{-1} for GBM, and 3260 cm^{-1} for HC (Figure 2b). The spectral differences between GBM and HC were further analysed for the 17 and 100K-uEVs at spectral regions associated with methyl bending (1400–1530 cm^{-1}), amide I stretching (1520–1840 cm^{-1}), methyl stretching (2700–3100 cm^{-1}), and carboxyl/primary amine/OH stretches (3000–3800 cm^{-1} ; Figure 2b). The 100K-uEV populations shared similar peak profiles across GBM and HC samples, however differences were observed in the 17K-uEV spectra. GBM 17K-uEVs had distinct methyl stretching peaks (2852 and 2917 cm^{-1}), which were absent in HC 17K-uEVs, and differences in the amide I peak intensities for β -pleated sheets and β -turns, compared to HC 17K-uEVs (Figure 2b). Interestingly, GBM uEVs contained at least 2-fold higher lipid to protein content, while HC 17K-uEVs were 4-fold more plentiful in protein content than lipid (Table 2). A PCA of the FT-IR data effectively distinguished GBM from HC uEV samples (Figure 2c).

3.4 | Proteome profiles and protein distributions across 100K-uEVs and 17K-uEVs can indicate a pre-operative GBM diagnosis

The size distributions of 100K-uEV and 17K-uEV subpopulations, determined by NTA, showed significantly smaller mean population sizes in PreOP GBM patients relative to HCs ($p \leq 0.02$; Figure S6A). Using DIA-MS/MS, we compared the proteomic content of 100K-uEVs and 17K-uEVs captured from GBM (PreOP, $n = 9$) and HC ($n = 13$) urine specimens. After filtering protein species to those identified in >80% of samples in each cohort, we detected 2499 and 2341 proteins in 100K-uEVs from PreOP GBM and HC samples, respectively, while 17K-uEVs had a total of 988 proteins in PreOP GBM and 1245 proteins in HCs (including top-100 EV proteins compiled in Vesiclepedia; Figure 3a). Pairwise comparisons between 100K-uEV and 17K-uEV proteomes identified 120 and 27 significant differentially abundant proteins in HC and GBM PreOP urine specimens, respectively ($FC \geq |2|$, adj p -value ≤ 0.05 ; Table S5). Among these, 22 proteins had overlapping significance in both HC and GBM PreOP specimens, all with the same direction of change (Figure 3b), that is, higher levels for 13 proteins (*ANXA11*, *CHMP4B*, *EPS8*, *GNG12*, *GPRC5B*, *IGHA1*, *LGALS3BP*, *PDCD6IP*, *PODXL*, *RAB7A*, *RPS27A*, *SDCBP* and *SLC44A2*) and reduced levels for nine proteins (*APOB*, *COL1A1*, *KRT1*, *KRT2*, *KRT5*, *KRT9*, *KRT10*, *LRPI* and *MYH10*) in 100K-uEVs relative to 17K-uEVs. Five uEV proteins were exclusively significant in GBM 100K-uEVs relative to 17K-uEVs, including higher levels of *ANXA7*, *CD2AP*, *RAB14* and *SHTN1*, and lower levels of *THOC2* (Figure 3b).

Next, we analysed the protein distribution changes between 100K-uEVs and 17K-uEVs in GBM. Relative protein abundance ratios were calculated for the 199 proteins shared between each pair of 100K-uEVs to 17K-uEVs (100K:17K, $n = 35$; Table S6). A student's t -test comparing 100K:17K ratios between PreOP GBM ($n = 9$) and HCs ($n = 13$), revealed 13 proteins (*AMBIP*, *ANXA5*, *APOA1*, *APOB*, *APOD*, *BROX*, *CAT*, *CNP*, *KNGL*, *MARCKSL1*, *MASP2*, *SERPINA5* and *TKT*) with significantly altered

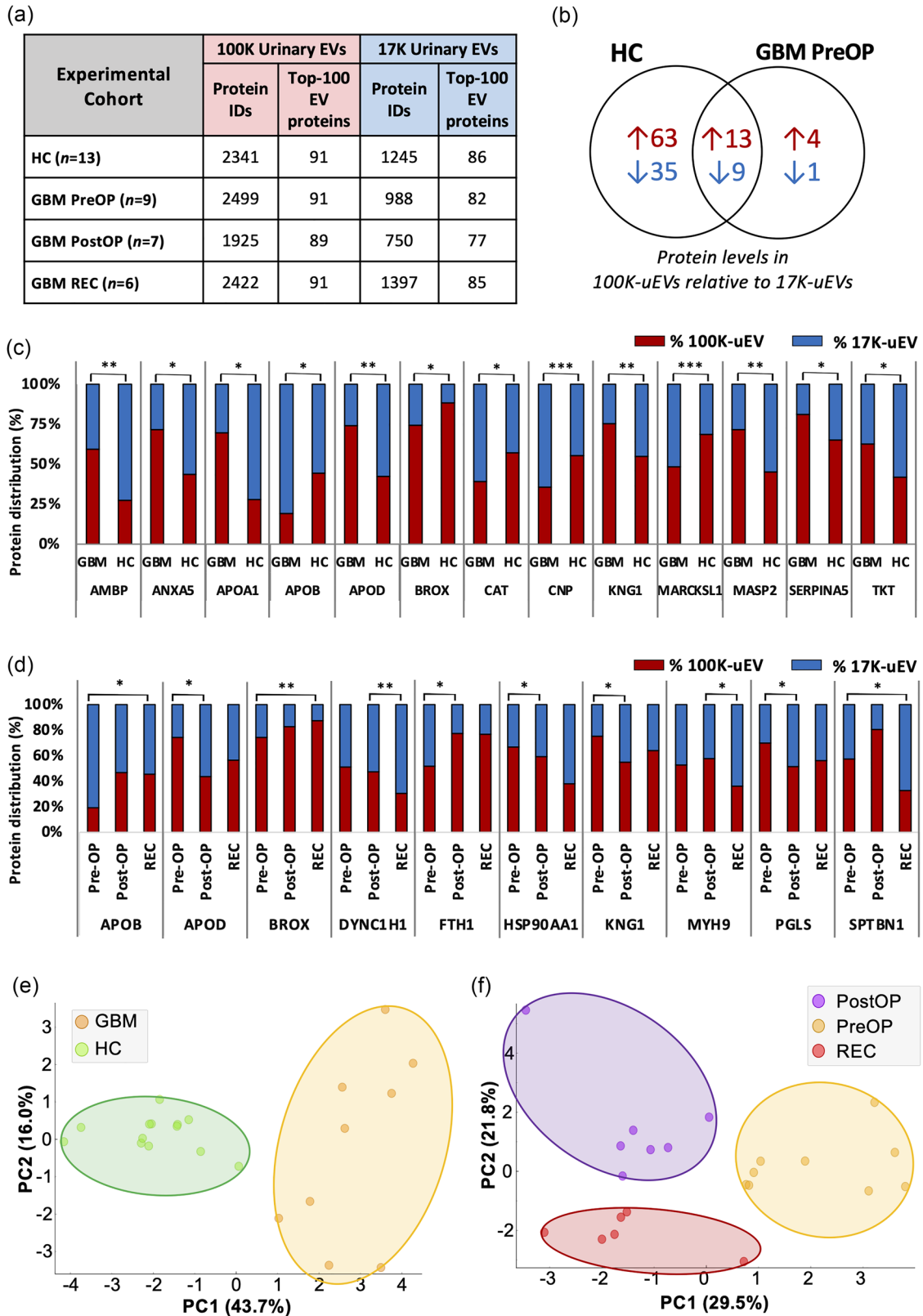


FIGURE 3 Changes in proteins distributed between 100K and 17K uEVs isolated from glioblastoma (GBM) patient urine. (a) The number of proteins identified by DIA-MS in more than 80% of 100K-uEVs and 17K-uEVs from GBM patients and healthy individuals (HCs), including top 100 EV marker proteins as reported by Vesiclepedia. (b) A Venn diagram showing 22 overlapping significant proteins in 100K-uEVs, relative to 17K-uEVs, for HCs and preoperative (PreOP) GBM patients; numbers of proteins with higher levels in red and lower levels in blue. (C–D) A stacked column plot illustrates the proportion of total protein (as a percentage), measured by DIA-MS, associated with 100K-uEVs (% red) and 17K-uEVs (% blue) for proteins with significantly changing

(Continues)

FIGURE 3 (Continued)

100K-uEV:17K-uEV protein abundance ratios between (c) GBM and HCs, and (d) across three GBM clinical timepoints [PreOP, post-operative (PostOP) and recurrence (REC)]. Principal component analyses (PCA) reveal clustering patterns based on 100K-uEV:17K-uEV abundance ratios for proteins with significant changes between (e) GBM and HC specimens (13 proteins), and (f) at the three GBM clinical timepoints (PreOP, PostOP and REC; 10 proteins). ^{‘*’} p -value < 0.05; ^{‘**’} p < 0.01; ^{‘***’} p < 0.001.

distribution (Table S6). These changes are visualised in a stacked column plot, which illustrates the percentage of each protein associated with 100K-uEVs and 17K-uEVs in both HC and GBM states (Figure 3c). For example, compared to 17K-uEVs, the 100K-uEVs captured from HCs carry lower levels of AMBP (0.37-fold), while 100K-uEVs from GBM patients carry significantly higher AMBP (1.45-fold). Interestingly, the distribution of these 13 proteins in 100 and 17K uEV samples can effectively distinguish GBM from HC specimens on PCA (Figure 3e). The corresponding average abundances values for these 13 proteins are also presented in Figure S5A and C.

3.5 | uEV protein distribution in GBM patients changes at distinct clinical timepoints

We then investigated changes in the levels of proteins identified in 100K-uEVs and 17K-uEVs from GBM urine captured pre-operatively (PreOP, $n = 9$), post-operatively (PostOP, $n = 7$) and at confirmed recurrence (REC, $n = 6$). Proteins confidently identified by DIA-MS in >80% of 100K-uEV and 17K-uEV samples from PreOP, PostOP and REC cohorts are tabulated in Figure 3a. Again, we interrogated the distribution of the 199 proteins common to all urine specimens by evaluating their abundance ratios (100K:17K) at different GBM clinical time points (Table S6). The levels of ten proteins (APOB, APOD, BROX, DYNCH1, FTH1, HSP90AA1, KNG1, MYH9, PGLS and SPTBN1) were found to be distributed differently in 100K-uEVs and 17K-uEVs at the different clinical time points (Figure 3d) and clearly separated GBM PreOP, PostOP and REC specimens on a PCA plot (Figure 3f). Of note, four of these differently distributed 100K:17K proteins (APOB, APOD, BROX, KNG1) also shared significant differences between GBM and HC samples (Figure 3c). The corresponding average abundances values for these ten proteins are also presented in Figures 5B and D.

3.6 | Large urinary-EV putative biomarker proteins corresponding to a GBM diagnosis and clinical changes

Next, we compared 17K-uEV proteomes captured from HC ($n = 13$) and GBM PreOP ($n = 9$) samples to identify differentially abundant 17K-uEV proteins significantly associated with a new GBM diagnosis. A total of 38 17K-uEV proteins changed between GBM PreOP and HC ($FC \geq |2|$, adjusted p -value < 0.05; Figure 4a; Table S7). Among these, 18 proteins overlapped with our previous study of 100K-uEVs in GBM (Hallal et al., 2024), demonstrating the same trends in abundance changes between GBM PreOP and HC samples. Functional analyses of the 38 17K-uEV proteins include positive associations for cancer, cellular stress and injury, neurotransmitters and other neurosignalling pathways, and negative associations to cytokine signalling and cellular immune response (Figure S6B).

ROC analyses were performed for the 38 significant 17K-uEV proteins; the AUCs are tabulated in Figure 4a, and confidence intervals are listed in Figure S6C. An L2-regularised logistic regression model was used to rank the importance of the 38 uEV proteins for distinguishing PreOP GBM from HC samples, based on their logistic regression coefficients (β , Figure S4A). A stepwise approach was then applied to the top-ranking proteins to identify the optimal combination of proteins for a multivariate logistic regression model that accurately differentiates GBM PreOP samples ($n = 9$) from HCs ($n = 13$). Across multiple stratified train-test data splits (75%–25%, 60%–40% and 50%–50%), the top seven proteins (SERBP1, KRT19, AARS1, LMAN2, KNG1, HPX and MYOF) consistently outperformed the full set of 38 significant proteins, and demonstrated superior performance across all metrics including AUC, classification accuracy, F1, precision, recall and specificity, and lower log loss values (Figure S7A–C). Training and testing log loss curves for the three data splits demonstrate the optimal performance of the models for both 38 proteins (Figure S8A) and the top seven protein set (Figure S8B), the latter showing lower training loss values.

The individual performances of the top seven proteins are visualised as ROC curves, showing high sensitivity and specificity ($AUC \geq 0.77$; Figure 4c), and their abundances in HC and PreOP GBM cohorts shown as boxplots (Figure 4d). The highest collective performance of the top seven 17K-uEV proteins was observed in the 75%–25% train-test split, achieving near-perfect classification accuracy of 98.2% (Figure 4b). Furthermore, the model’s generalisability was evaluated on an independent blinded hold-out set of four GBM PreOP and four HC specimens (Figure 4c). The model had a high classification accuracy of 87.5% (Figure 4c-1) and could correctly predict 75% of GBM (3/4) samples and 100% of HCs (4/4). A PCA based on the abundance levels of the top performing protein set shows distinct separation between GBM PreOP and HC samples (Figure 4f).

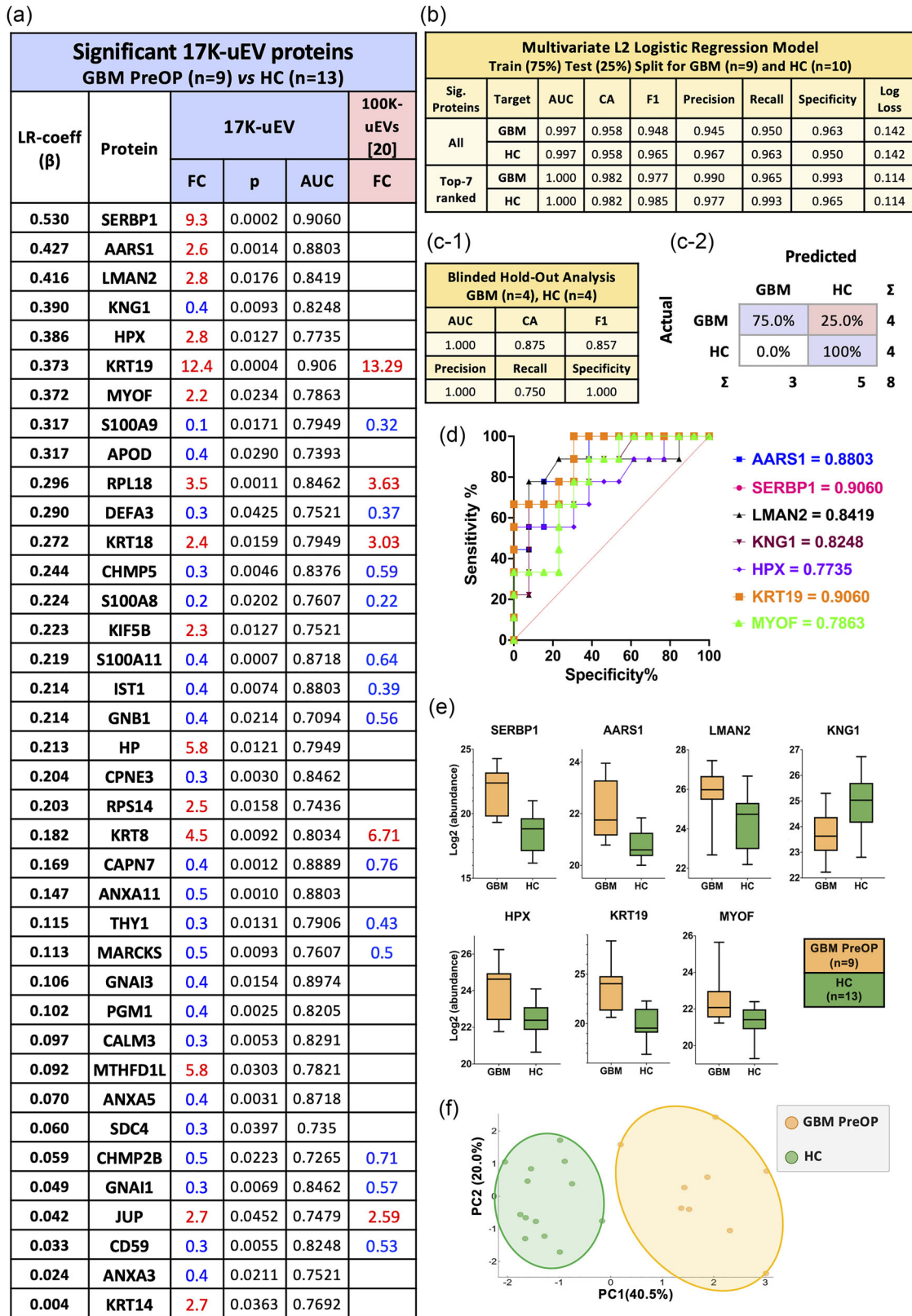


FIGURE 4 Putative diagnostic biomarkers for Pre-Operative (PreOP) GBM in the 17K uEV pellet. (a) The table of 38 differentially abundant proteins in the 17K-uEV fraction in PreOP GBM patients relative to HCs, including fold-changes (FC), p-values, L2-regularised logistic regression coefficients (LR-coeff β) ranked by order of importance, and the area under the Receiver Operating Characteristic (ROC) curve (AUC). Notably, 18 proteins were also significant putative diagnostic GBM biomarkers associated with 100K-uEVs (Hallal et al., 2024), all of which exhibited the same direction of change. (b) A stepwise approach using the top-ranked proteins scored by a logistic regression model, identified seven proteins that optimally classified PreOP GBM ($n = 9$) from HCs ($n = 10$). A multivariate L2-regularised logistic regression model (stratified 75%-train, 25%-test split, repeated 100 times) showed superior performance metrics for the top seven proteins (SERBP1, AARS1, LMAN2, KNG1, HPX, KRT19 and MYOF) with an AUC = 1.000; classification accuracy (CA) = 98.2%, F1 = 99.7%,

(Continues)

FIGURE 4 (Continued)

Precision = 99.0%, Recall = 96.5%, Specificity = 99.3% and Log Loss = 0.114. These seven proteins were selected as the most important classifiers for differentiating PreOP GBMs from HCs. The model's predictive performance was further evaluated on an (c-1) independent blinded hold-out set of PreOP GBM ($n = 4$) and HC ($n = 4$) samples, showing classification accuracy of 87.5% and recall of 75.0%. (c-2) A confusion matrix showed the percentage of correctly classified GBM and HC samples by the seven-protein model. (d) ROCs for all seven proteins and their respective AUC values. (e) Box and whisker plots of the seven panel proteins illustrate their expression distribution for PreOP GBM ($n = 9$) and HC ($n = 13$) specimens. The whiskers represent the full range of the protein abundance (minimum–maximum), and the middle line represents the median. (f) The expression levels of the seven top performing 17K-uEV proteins show clear separation of PreOP GBM ($n = 9$) and HC samples ($n = 13$) on PCA analysis.

We further evaluated 17K-uEV proteome changes across samples collected at three GBM clinical timepoints (PreOP, PostOP and REC; Table 1). Significant differentially abundant proteins identified in pair-wise comparisons (PreOP vs. PostOP, PostOP vs. REC, PreOP vs. REC) are tabulated in Table S7. Significant 17K-uEV proteins corresponding to 'GBM tumour burden' (PreOP vs. PostOP), included SMC1A, SPTA1, MYH9, CNDP2, ADH5, PDIA3, MAT2A, YWHAG, TGM2, MYO6, HSP90AB1 and EFEMP1. Interestingly, three proteins (CNDP2, HSP90AB1 and MYH9) increased in PreOP samples, which were also significantly higher in PreOP than in HC samples (Figure 5a, Table S7). We identified 36 significant 17K-uEV protein changes corresponding to 'GBM recurrence' (PostOP vs. REC) and 24 17K-uEV proteins corresponding to 'treatment resistance' (PreOP vs. REC). We observed overlapping proteins (MAT2A, SMC1A and ADH5) with significant changes in the 'tumour burden' and 'GBM recurrence' analyses, with similar abundance levels in the urine of patients with a high tumour load (i.e., PreOP and REC; Figure 5b). Ten overlapping significant proteins were also observed in the 'GBM recurrence' and 'treatment resistance' comparisons (AARS1, ANXA4, ANXA5, GPI, MARKCSL1, MYOF, AKAP13, HSP90AAS1, PLCD1 and PLEC), all following the same direction of change with significantly altered levels at REC compared to PreOP and PostOP urine (Figure 5c). Significantly changing proteins identified here in uEVs that were also previously described in the small-EV populations of other GBM body fluids are listed in Table 3.

4 | DISCUSSION

4.1 | Classification and composition of small and large urinary EV populations

uEV isolates were separated by differential centrifugation at $17,000 \times g$ (17K-uEVs) and $100,000 \times g$ (100K-uEVs), and their size ranges (80–600 nm and 80–400 nm, respectively) were measured by NTA (Figure 1c). Previously, large EVs isolated through high-speed centrifugation ($10,000$ – $20,000 \times g$) were classified as plasma membrane-derived 'microvesicles', while small EVs isolated through ultracentrifugation ($100,000$ – $200,000 \times g$) were associated with endosomal-derived 'exosomes'. However, recent research has challenged this distinction, and EVs are now appreciated for their remarkable diversity in terms of size, morphology, and cargo. This study explores the compositional differences between the uEV populations based on their physical size only, and no assumptions have been made regarding their biogenic or cellular origin. Contradictory definitions have plagued EV classification, particularly for subtypes such as exosomes and microvesicles, which can be both small (<200 nm) and large (200–1000 nm), often co-purify with non-vesicular particles, and are influenced by their source cell types (Tkach et al., 2018; Zhang & Lyden, 2019; Zhang et al., 2021). In our study, while 17K-uEVs and 100K-uEVs exhibited distinct EV peak populations (Figure 1c), both populations shared a size distribution ranging from 80 to 300 nm. Despite this overlap in size, our proteomic analyses revealed 484 proteins uniquely present in all 100K-uEV samples (Figure 1d, Table S4), suggesting that 100K-uEVs include EV populations distinct from 17K-uEVs. Proteins restricted to 100K-uEVs include known EV-markers, CD9, CD63, CD81, TSG101, ITGB1 and RAB proteins, which are widely reported in both exosomal and microvesicle populations (Haraszti et al., 2016; Merchant et al., 2017). Conversely, six proteins were exclusively identified in all 17K-uEV samples, including ATP6API, KRT18, LAIR1, SERPINA3, VASN and KPNB1 (Table S4) that are all reported in both exosome and microvesicle studies (Ayre et al., 2017; Bui et al., 2022; Hayashi et al., 2020; Liao et al., 2022; Vitale et al., 2021; Yang et al., 2017), except LAIR1 which was reported in plasma-membrane derived ectosomes (Kalra et al., 2016).

While the proteomic differences elucidated in our study cannot be attributed to exact EV biogenesis mechanisms and EV origin, our functional annotation of resolved EV proteomes revealed that a higher percentage of 17K-uEVs proteins (98.50%) were annotated to the urinary compartment compared to 100K-uEV proteins (86.94%), perhaps suggesting that smaller uEVs originate from broader anatomical sources (Figure 1e-2). Multiple routes have been proposed for small uEV entry into the urine, yet the mode by which larger uEVs enter the urine is poorly understood. Given that a significant portion (97%) of the 17K-uEV proteome is annotated to the plasma, it is plausible that larger uEVs are encapsulated and packaged during the filtration process (Erdbrügger et al., 2021; Kerjaschki et al., 1989; Londono & Bendayan, 2005; Musante et al., 2020; Ndisang, 2018; Patrakka et al., 2002).

The biomolecular compositions of 100K-uEVs and 17K-uEVs, detected by FT-IR analysis, showed similar spectral profiles that are typical for nucleic acids, carbohydrates, lipid/acyl chains and protein/peptides in the uEV populations of HCs (Figure 2a), that

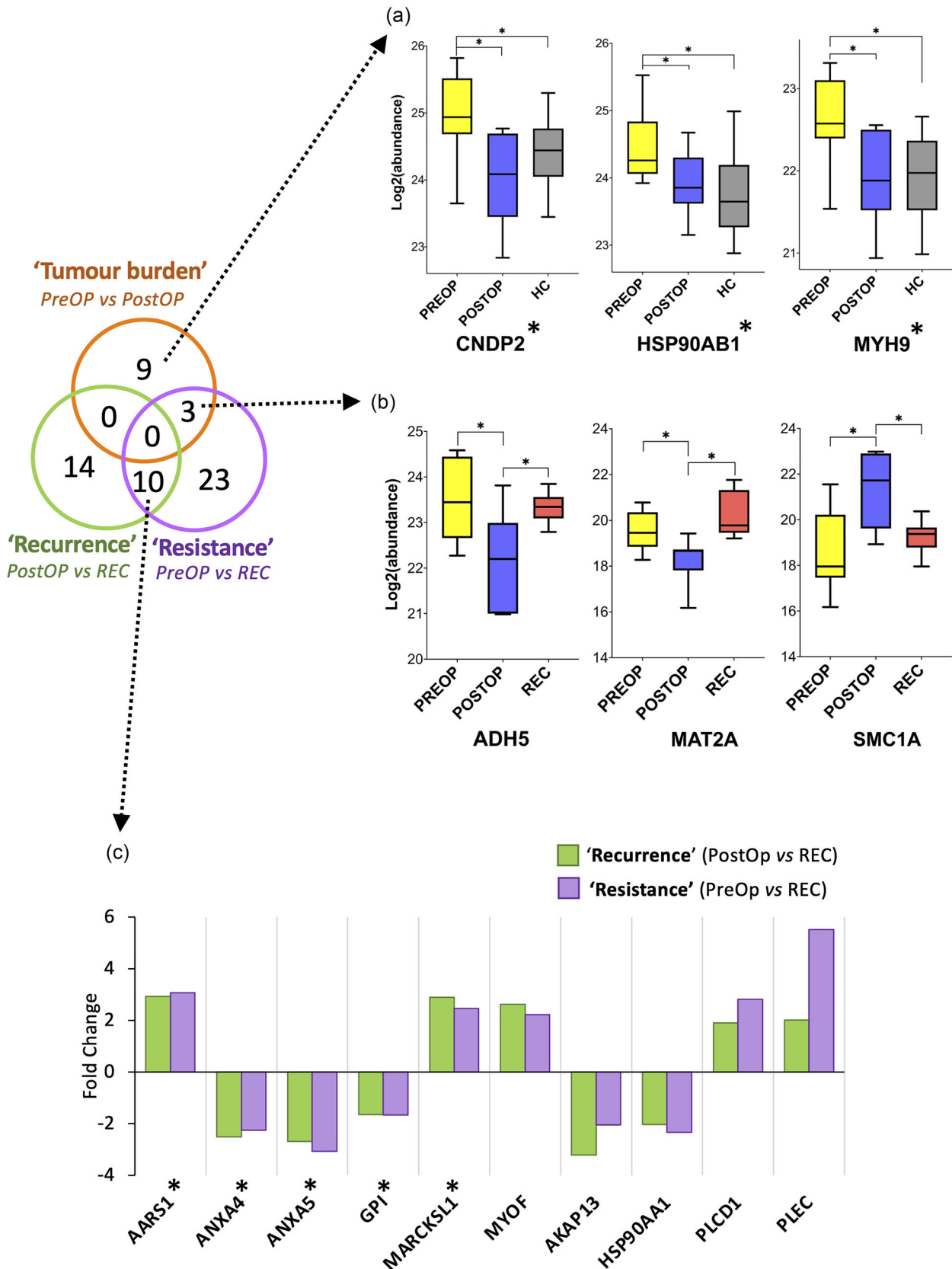


FIGURE 5 Protein changes in 17K-uEVs across three GBM clinical timepoints. The Venn diagram depicts the overlap of significant 17K-uEV protein changes in pairwise comparisons between PreOP, PostOP and REC urine samples. (a) Box and whiskers plots show the expression of three GBM 'tumour burden' proteins CNDP2, HSP90AB1 and MYH9 that were also significantly changed between PreOP and HC samples. (b) Box and whiskers plot show the expression of proteins (MAT2A, SMC1A, ADH5) with significance in both GBM 'tumour burden' and 'recurrence' signatures. The protein abundance for each cohort is plotted as log2(abundance), the upper error bars signify the maximum, lower error bars represent the minimum, and the middle line represents the

(Continues)

TABLE 3 Summary of significantly changing uEV proteins previously identified in small-EV populations captured from other GBM patient biofluids including urine (Hallal et al., 2024), ex vivo neurosurgical 'CUSA' aspirates (GBM vs. glioma IDH-mut WHO grades 2-3) (Hallal, Russell et al., 2019), peripheral plasma (GBM vs. cancer and non-cancer controls) (Hallal, Azimi et al., 2020) and GBM culture media in vitro (Mallawaarachy et al., 2017). Significant proteins specific to GBM-EVs isolated from neurosurgical aspirates and plasma are denoted (*).

Gene name	Protein name	Significant study finding Distribution between 100K and 17K uEVs	17K pellet	Significant in other GBM-EV studies
AMBIP	Protein AMBP	GBM vs. HC	GBM vs. HC	Urine
ANXA3	Annexin A3			Urine
APOAI	Apolipoprotein A1	GBM vs. HC		CUSA
APOD	Apolipoprotein D	GBM vs. HC tumour burden		Urine
BASPI	Brain acid soluble protein		Recurrence	Urine
BROX *	BRO1 domain-containing protein BROX	GBM vs. HC resistance		Urine, Plasma
CAPN7	Calpain-7		GBM vs. HC	Urine
CAPS	Calcium-dependent secretion activator 1		Recurrence	Urine
CD59 *	CD59 glycoprotein		GBM vs. HC	Urine, CUSA
CHMP2B	Charged multivesicular body protein 2b		GBM vs. HC	Urine
CHMP5	Charged multivesicular body protein 5		GBM vs. HC	Urine
CNP	2',3'-cyclic-nucleotide 3'-phosphodiesterase	GBM vs. HC		Urine
COLL1A1	Collagen alpha-1(I) chain		Recurrence	Urine
CPNE3	Copine-3		GBM vs. HC	Urine
DEFA3 *	Neutrophil defensin 3		GBM vs. HC	Urine, CUSA
DYNC1H1	Cytoplasmic dynein 1 heavy chain 1	Recurrence		Cell culture
FABP5 *	Fatty acid-binding protein 5		Recurrence	Urine, CUSA
FLNA *	Filamin-A		Recurrence	CUSA, Cell culture
FTH1	Ferritin heavy chain	Tumour burden		Urine
GNAI1	Guanine nucleotide-binding protein G(i) subunit alpha-1		GBM vs. HC	Urine
GNBI	Guanine nucleotide-binding protein G(1)/G(S)/G(T) subunit beta-1		GBM vs. HC	Urine
HP*	Haptoglobin		GBM vs. HC	CUSA
HSP90AA1*	Heat shock protein HSP 90-alpha	Tumour burden		Urine, Cell culture, CUSA
ISTI	ISTI homolog		GBM vs. HC	Urine
JUP	Junction plakoglobin		GBM vs. HC	Urine
KRT18	Keratin, type I cytoskeletal 18		GBM vs. HC	Urine
KRT19	Keratin, type I cytoskeletal 19		GBM vs. HC	Urine
MARCKS	Myristoylated alanine-rich C-kinase substrate		GBM vs. HC	Urine

(Continues)

TABLE 3 (Continued)

MARCKSL1	MARCKS-related protein	GBM vs. HC	Resistance	Urine
MAT2A	S-adenosylmethionine synthase isoform type-2		Tumour burden recurrence	Urine
MTHFD1*	C-1-tetrahydrofolate synthase, cytoplasmic		Recurrence	CUSA
MYOF*	Myoferlin		GBM vs. HC recurrence resistance	Urine, CUSA
MYH9 *	Myosin-9	Recurrence		Urine, Cell culture
NEFH	Neurofilament heavy polypeptide		Recurrence	Urine
PFKL	ATP-dependent 6-phosphofructokinase, liver type		Recurrence	Urine
PLCD1	1-phosphatidylinositol 4,5-bisphosphate phosphodiesterase delta-1		Recurrence	Urine
PLEC	Plectin		Recurrence resistance	Cell culture
PSMA1	Proteasome subunit alpha type-1		Resistance	Urine, Cell culture
PYGB	Glycogen phosphorylase, brain form		Recurrence	Cell culture
RPL18	Large ribosomal subunit protein eL18		GBM vs. HC	Urine
SI00A11*	Protein SI00-A11		GBM vs. HC	Urine, CUSA
SI00A8	Protein SI00-A8		GBM vs. HC	Urine
SI00A9	Protein SI00-A9		GBM vs. HC	Urine
SERP1	SERPINE1 mRNA-binding protein 1		GBM vs. HC	Plasma
THY1	Thy-1 membrane glycoprotein		GBM vs. HC	Urine
TPP1	Tripeptidyl-peptidase 1		Recurrence	Urine
TKT	Transketolase	GBM vs. HC	Recurrence	Cell culture
YWHAG	14-3-3 protein gamma		Tumour burden	Cell culture

FIGURE 5 (Continued)

median; * p -value < 0.05. (c) The fold changes of the ten shared GBM 'recurrence' and 'resistance' proteins show the same expression trends. Proteins denoted by an asterisk (*) are also related to GBM with significance between GBM PreOP and HC.

also resemble previous studies of prostate cancer uEVs (Yap et al., 2019), hepatocellular carcinoma serum-EVs (Di Santo et al., 2022) and melanoma cell-EVs (Stepień et al., 2021). To extrapolate meaningful differences between 100K-uEVs and 17K-uEVs, we selected non-overlapping FT-IR regions for lipids (1458–1465 cm^{-1} and 2700–3000 cm^{-1}) and amide I for proteins (1600–1700 cm^{-1}) for further qualitative and quantitative assessment (Figure 2a). Expectedly, both 100K-uEVs and 17K-uEVs showed prominent peaks in the methyl bending region (1458–1465 cm^{-1}) that is primarily related to the polar head group of lipids and fatty acid/acyl chains of phospholipids (Portaccio et al., 2023). However, only 100K-uEVs had signals corresponding to methyl stretching (2700–3000 cm^{-1}) associated with lipid hydrocarbon chains, which contributed to the striking difference observed in measured lipid-to-protein content of 17K-uEVs (Figure S4). Studies consistently report that small and large EV populations possess a lipid bilayer rich in sphingomyelin, cholesterol, and saturated phospholipids, providing membrane stability and delaying EV degradation in biological fluids (Hallal et al., 2022; Paolino et al., 2022). As most lipids, for example, phospholipids, triacylglycerols, and sterols, exhibit peaks in the 2700–3000 cm^{-1} region (Movasaghi et al., 2008; Portaccio et al., 2023), we found this observation puzzling. The absence of methyl stretches in 17K-uEVs contradicts a previous FT-IR study that reported clear methyl stretching profiles for large EVs derived from cultured normal human melanocytes and melanoma cells (Stepień et al., 2021). This disparity could be explained by shorter acyl chain lengths and disordered conformational phases that contribute to less prominent and broader FT-IR spectral peaks (Christy & Egeberg, 2006; Derenne et al., 2013; Lewis & McElhaney, 2013) or other inherent lipidomic differences between uEVs and EVs from other biofluids. Regardless, further lipidomic investigations are needed for a more comprehensive understanding of this FT-IR anomaly.

Also of note, and worthy of further investigation, is the contrasting observations in secondary protein conformations with enrichments of β -turns in 100K-uEVs and β -pleated sheets in 17K-uEVs (Table 2). While inferences to protein conformational differences in complex proteomics data is exceedingly difficult, this observation may broadly reflect the different classes of proteins cargoed in EV subtypes. β -turns are usually, but not invariably, found on the water accessible surface of proteins, and account for about a third of the structure of globular proteins. Indeed, tightly compact globular proteins tend to have more β -turns than elongated fibrous proteins, which are often predominantly comprised of β -sheet structures (Rose et al., 2004). In line with this, we identified triple the number of protein species associated with 100K-uEVs, that is, 683 proteins compared to 205 in 17K-uEVs (Figure 1d), that feasibly would need more compact structural forms for packaging in physically smaller vesicles. Further, we detected significantly higher levels of fibrous protein types, including KRT1, KRT2, KRT5, KRT9, KRT10, in 17K-uEVs (Figure 1f) that may help account for the greater relative proportion of β -sheet structures in these EV populations.

4.2 | The biomolecular composition of uEVs in GBM patients

FT-IR analyses of uEVs captured from PreOP GBM patients revealed prominent alterations in methyl bending, methyl stretching, amide I and carboxyl/primary amine/OH stretches. The most notable changes across all four vibrational regions were observed in GBM 17K-uEVs, specifically in methyl stretching peaks that were absent in HC 17K-uEVs (Figure 2b). These alterations may reflect changes in GBM 17K-uEV lipid profiles, conformations, molecular packing, and protein-lipid interactions. Similar changes have been reported in Raman spectra of serum-EVs, with cancer specimens showing stronger lipid bands in the 2750–3040 cm^{-1} compared to healthy samples (Uthamacumaran et al., 2022). Machine learning analysis of the serum-EV spectra also demonstrated high accuracy for distinguishing cancer from healthy samples, with Raman spectra providing better predictive power than FT-IR spectra (Uthamacumaran et al., 2022). Further elucidation of the biomolecular changes in GBM 17K-uEVs requires comprehensive lipidomic assessments to determine the compositional alterations (Brzozowski et al., 2018), coupled with nuclear magnetic resonance (NMR) spectroscopy to assess structural dynamics and protein-lipid interactions (Alexandri et al., 2017). More broadly, recent reports indicate that lipid metabolism reprogramming is a hallmark of GBM pathophysiology, and targeting lipid de novo synthesis, uptake, storage and catabolism pathways may be key to a successful therapeutic outcome (Kou et al., 2022). At the same time, it is conceivable that highly destructive glioblastoma tumours invading lipid-rich brain tissue would leach lipid metabolite species into the circulation, which may be useful as biomarkers. While the promise of serum lipidomics for glioblastoma biomarker discovery has been proposed (Soylemez et al., 2023; Yu & Aboud, 2024), there is considerable scope to explore other biofluid compartments, including urine and EVs.

We extensively characterised the 100K-uEV and 17K-uEV proteomes from GBM and HCs using our previously established DIA-MS method (Hallal, Azimi et al., 2020) and resolved 13 proteins (AMBP, ANXA5, APOA1, APOB, APOD, BROX, CAT, CNP, KNG1, MARCKSL1, MASP2, SERPINA5 and TKT) with significant distributional changes in GBM between 100K-uEVs and 17K-uEVs (Figure 3c). Particularly noteworthy were shifts in the distributions of APOB, APOD, BROX and KNG1 proteins between uEV subpopulations across different GBM clinical time points (Figure 3d). Little is known about the exact composition

of EV sub-populations and how they may be influenced by malignancy; however, our findings highlight the dynamic nature of uEVs potentially reflecting clinically significant parameters like tumour recurrence and therapy response.

Previous studies have suggested that membrane protein expression correlates with EV size (Zhai et al., 2023), and different EV populations carry distinct cancer-specific proteomes and oncogenic cargo with biomarker potential (Ahmadzade et al., 2023). Moreover, differential secretion rates of s-EVs and l-EVs from GBM cells (U87MG-EGFR^{III}) have been demonstrated, with GBM cells secreting more l-EVs containing EGFR^{III} protein into the circulation of GBM-bearing mice, relative to non-cancerous cells (Yekula et al., 2019). Although we do not report higher quantities of EVs from the 17K pellet from GBM patient urine, the pronounced FT-IR spectral and proteomic differences of 17K-uEVs may be attributed to alterations in EV biogenesis and selective packaging, increased l-EV secretion rates from GBM tumours into the peripheral blood, as well as changes in the urogenital tract response to tumour and treatment that might facilitate l-EV passage and secretion into the urine.

4.3 | Streamline urine processing for measuring clinically relevant GBM l-uEV biomarkers

Most urinary EV studies to date have sought to resolve novel biomarkers associated with s-uEVs or 100,000 × *g* pellets, ignoring or discarding l-uEVs or 17,000 × *g* EV populations that are often collected as at an interim protocol step (Musante et al., 2020). We recently reported potential biomarkers for diagnosing and monitoring GBM s-uEVs (Hallal et al., 2024), and have extended our study to assess the GBM biomarker potential of uEVs in the 17,000 × *g* pellet. It is important to note that relatively small volumes of urine are indicated for characterisation and molecular analyses of larger uEVs, including 0.5 mL for EV enumeration and microRNA quantification by qPCR, 1.5–4.5 mL for flow cytometry, and 4.5 mL for proteomic assessments by immunoblotting (Musante et al., 2020). At these volumes, bench-top centrifuges within diagnostic laboratories can readily pellet larger uEV populations at 17,000 × *g* in only 30 min.

We identified 38 17K-uEV proteins with significant abundance changes between primary GBM PreOP patients and HCs (Figure 4a). Among these, eighteen proteins were previously identified in our s-uEV proteomics study that also corresponded to a PreOP GBM diagnosis, including KRT19, S100A9, RPL18, DEFA3, KRT18, CHMP5, S100A8, S100A11, IST1, GNBI, KRT8, CAPN7, THY1, MARCKS, CHMP2B, GNAI1, JUP and CD59, with all shared markers displaying the same direction of change in both uEV populations of GBM PreOP patients (Figure 4a, Hallal et al., 2024). Additionally, ANXA5, APOD and KNG1 proteins displayed significant differential distribution between 100K-uEVs and 17K-uEVs from GBM patients before and after surgery (Figure 3c,d). Notably, we also identified top-performing GBM diagnostic markers (SERPBI, AARSI, LMAN2, KNG1, HPX, KRT19 and MYOF) in the 17K-uEV pellet that demonstrated near-perfect cumulative accuracy (AUC = 1.000; classification accuracy = 98.2%) using a logistic regression model (Figure 4b). The model was also generalisable to a small set of hold-out PreOP GBM specimens (*n* = 4) and HCs (*n* = 4), with a classification accuracy of 87.5% (Figure 4c-1). While several significant proteins were shared between 100K-uEVs and 17K-uEVs, only KRT19 was common between the 17K-uEV GBM PreOP signature and our previously reported s-uEV GBM diagnostic signature (KRT19, RPS2, IST1, RPL18, RPL28, CSTB, ALDH3B1, RPL7A and GNAI2) (Hallal et al., 2024), indicating that separate uEV fractions offer distinct, however complementary, biomarker potential.

Remarkably, all seven 17K-uEV proteins (SERPBI, AARSI, LMAN2, KNG1, HPX, KRT19 and MYOF) that were able to accurately classify the PreOP GBM from HC specimens are implicated in aspects of cancer biology, including GBM pathogenesis. Among these, AARSI (alanyl-tRNA synthetase 1) acts as a lactyltransferase and intracellular lactate sensor that plays key roles in onco-regulation (Zong et al., 2024), and forms a positive feedback loop with YAP-TEAD oncoproteins and modulates the Hippo pathway (Ju et al., 2024). While the precise role of AARSI in GBM remains unclear, the overexpression of the YAP-TAZ-TEAD complex deregulates the Hippo pathway in glioma progression, and activates chemoresistance mechanisms such as DNA repair and the development of an immunosuppressive microenvironment (Casati et al., 2021; Liu et al., 2019; Tian et al., 2015). Additionally, elevated SERPBI (SERPINE1 mRNA Binding Protein 1) is prevalent in GBM tumour tissue and regulates glioblastoma development through epigenetic regulation (Kosti et al., 2020). Our previous research measured elevated SERPBI levels in GBM patient plasma-EVs, relative to cancer and non-cancer controls (Hallal, Azimi et al., 2020), corroborating the observed increase of SERPBI in 17K-uEVs from GBM patients here. Interestingly, multiple calcium-binding proteins were significant in PreOP GBM 17K-uEVs, which are known to be dysregulated in glioblastoma tissue and play important roles in tumour cell proliferation and metastasis (Polisetty et al., 2012). This included LMAN2 (lectin, mannanose binding 2), along with notably lower levels of S100 proteins (A8, A9 and A11) and ANAX5 (Figure 4). KNG1 (Kininogen 1) is downregulated in GBM tumour tissue and serum, associated with shorter patient survival times and reported to suppress glioma progression (Xu et al., 2018). Here, significantly reduced KNG1 levels were detected in GBM 17K-uEVs compared to HCs (Figures 3 and 4). Elevated HPX (hemopexin) is part of an eight-gene signature that distinguishes GBM tumours from healthy brain tissues and has prognostic significance (Yuan et al., 2022). Keratin proteins, particularly KRT19, play important roles in cancer invasion (Saha et al., 2017); high levels of hypomethylated KRT19 in GBM tumours is negative marker for survival (Mao et al., 2020). Finally, elevated MYOF (Myoferlin), one of the 17K-uEV protein classifiers for PreOP GBM, is frequently overexpressed in cancer, and promotes cancer cell migration and invasion (Blomme et al., 2016; Eisenberg et al., 2011). Moreover, MYOF is described as a critical component of cancer-derived

EVs, significantly influencing tumour growth by enhancing EV functionality, facilitating molecular transfer and maintaining EV size (Blomme et al., 2016).

We further evaluated 17K-uEV protein changes across discrete GBM clinical time points, revealing trends that correspond to GBM tumour burden, recurrence, and resistance. Specifically, CNDP2, HSP90AB1, and MYH9 were identified as significant GBM diagnostic proteins (GBM PreOP vs. HC) and were also associated with *tumour burden* (GBM PreOP vs. PostOP), with higher levels corresponding to a high tumour load (Figure 5b). Like our 100K-uEV investigation (Hallal et al., 2024), differentially abundant proteins related to a GBM diagnosis (GBM PreOP vs HC), and tumour burden (PreOP vs PostOP) shared the same direction of change. While the surgical procedure alone may have influenced these proteomic changes (Finnerty et al., 2013), significant protein markers are annotated to activated cancer pathways, suggesting some functional relevance (Figure S6B). However, these significant changes could also be secondary to systemic inflammation or other GBM-related pathophysiological effects. Additionally, longitudinal assessments of uEVs from patients with neurological disorders have indicated stable relative abundances of uEV profiles within individuals over several weeks (Wang et al., 2019), supporting the notion that measuring uEV biomarkers at distinct clinical intervals may allow non-invasive indications of GBM tumour changes in situ.

4.4 | Study limitations and future directions

As urine production fluctuates considerably to maintain water, ion, and pH homeostasis, uEVs are more variable than EVs from the blood and other body fluids (Erdbrügger et al., 2021). uEV research is still in its infancy, and there is an absence of standardised methods to adjust for confounding factors including the EV excretion rate and variations in uEV isolation. Current uEV normalisation approaches include adjusting for excretion rates based on absolute (total protein, uEV number or levels of uEV biomarkers) or relative (collection time, urinary creatinine and osmolality) measurements (Erdbrügger et al., 2021). As the uEV field matures, normalisation strategies will become better defined and more accurate. To facilitate future analysis and contextualisation of our EV data by other researchers, we have included relevant blood biochemistry and urinary creatinine and protein levels, as recommended by MISEV2023 (Welsh et al., 2024), in Table S1. In our proteomic investigation, we adopted a global absolute normalisation method, conducting DIA-MS analyses on equal amounts of total uEV proteins, which were then normalised using quantile normalisation to account for differences in sample size and measurement bias.

While the precise contributions of different components of the urogenital tract to the total uEV population are not yet fully understood (Erdbrügger et al., 2021), it is plausible that external factors such as damage, injury, infection, or inflammation within and beyond the urogenital system can influence both the total excretion of uEVs and the composition of the uEV pool. For example, procedures like digital rectal examinations can impact uEV composition, resulting in higher levels of prostatic fluids and EVs derived from the prostatic luminal epithelium (Hendriks et al., 2016). In our study, the effect of catheterisation on uEVs from GBM patients analysed here cannot be discounted (Peychl & Zalud, 2008), and significant findings from comparisons between uEVs from catheterised GBM patients and voided HCs should be carefully validated in our future investigations. Furthermore, GBM patients undergoing therapy may experience microscopic haematuria due to myelosuppression, which contributes to a bleeding tendency and a weakened immune system with increased risk of urological infections (Furukawa et al., 2018). The presence of blood in the urine from patients experiencing haematuria can cause uEV aggregation and loss, leading to false high ratios of protein-to-creatinine, which can negatively impact molecular assessments (Raimondo et al., 2018). Thus, our future studies will also report the blood content in urine specimens to identify patients with haematuria complications and ensure minimal impact on our uEV molecular assessments. Furthermore, our future uEV studies may benefit from implementing mild trypsin treatments of patient urine prior to uEV isolation, as this has been shown to reduce blood protein contaminants and enhance uEV proteomic assessments (Raimondo et al., 2018). Addressing these challenges will ensure that resolved uEV cargoed biomarkers in this study are unaffected by complications that are frequently associated with aggressive brain tumours, treatment response or toxicity.

Given the essential role of lipids in uEVs and the limited existing lipidomic characterisation studies (Erdbrügger et al., 2021), coupled with noteworthy differences observed in the FT-IR spectral regions associated with lipids for GBM 17K-uEVs, future comprehensive lipidomic investigations of both 100K-uEVs and 17K-uEVs are warranted. Mass spectrometry assessments will enable a comparative assessment of lipid species across 100K-uEVs and 17K-uEVs, while techniques such as NMR will provide insight into their structural dynamics and interactions with proteins (Alexandri et al., 2017; Brzozowski et al., 2018). It is important to note that while no differences in nucleic acid or carbohydrate content were observed in the FT-IR assessments between uEV populations from HCs, we could not make these observations in our GBM uEVs due to the presence of PBS in our samples. Furthermore, considering the significant differences in protein distribution between 100K-uEVs and 17K-uEVs in GBM, along with the feasibility of 17K-uEVs for liquid biopsies that detect tumour burden, recurrence and treatment resistance, further exploration of both 100K-uEVs and previously overlooked 17K-uEVs as sources of biomarkers is justified. Our future validation investigations will encompass larger, longitudinal cohorts of urine samples captured from GBM patients at multiple clinical time points, including at treatment baseline, end-of-treatment, and instances of confirmed tumour recurrence or pseudoprogression. To ensure the validity and specificity of findings to GBM patients, future studies also require the expansion of specimen cohorts

to include cancer controls and non-cancer controls. Accompanying rich clinical and radiological metadata will allow us to validate and assess the clinical utility of biomarkers cargoed by 100K-uEVs and 17K-uEVs, providing deeper insights into uEV subpopulation dynamics in GBM patients.

4.5 | Concluding remarks

While the promise of uEVs in biomarker discovery is emerging, little is known about the characteristics and composition of different urinary EV subpopulations, as well as their relevance as biomarkers. In this study, we conducted the first comprehensive characterisation of EV fractions obtained at $100,000 \times g$ and $17,000 \times g$ from urine. We found clear differences in protein and lipid content between these populations, which enabled differentiation between patients with GBM and HCs. Using our established DIA-MS method (Hallal et al., 2024), we performed in-depth proteomic profiling of both 100K-uEVs and 17K-uEVs, revealing significant proteome distribution changes in GBM patient urine and across distinct GBM clinical time points. We identified potential 17K-uEV protein biomarkers associated with a GBM diagnosis that are distinct from 100K-uEV diagnostic biomarkers previously determined for GBM (Hallal et al., 2024). These findings highlight the biomarker potential of uEV populations for a GBM diagnosis, monitoring tumour progression and response to treatment. Further research is warranted to fully appreciate the individual and combined capabilities of biomarkers associated with different uEV populations.

AUTHOR CONTRIBUTIONS

Susannah M. Hallal: Conceptualization (equal); data curation (lead); formal analysis (lead); investigation (equal); methodology (equal); visualization (equal); writing—original draft (equal); writing—review & editing (equal). **Liam A. Sida:** Data curation (supporting); formal analysis (supporting). **Ágota Túzesi:** Methodology (supporting); writing—review and editing (supporting). **Brindha Shivalingam:** Resources (supporting); writing—review and editing (supporting). **Hao-Wen Sim:** Investigation (supporting); resources (supporting); writing—review and editing (supporting). **Michael E. Buckland:** Resources (supporting); supervision (supporting); writing—review and editing (supporting). **Laveniya Satgunaseelan:** Conceptualization (supporting); methodology (supporting); resources (supporting); writing—review and editing (supporting). **Kimberley L. Alexander:** Conceptualization (lead); data curation (equal); formal analysis (equal); funding acquisition (lead); investigation (lead); project administration (lead); resources (lead); supervision (lead); visualization (equal); writing—original draft (equal); writing—review and editing (lead).

ACKNOWLEDGEMENTS

Urine samples and associated information were provided by the Sydney Brain Tumour Bank at Royal Prince Alfred Hospital and Chris O'Brien Lifehouse. Thank you to all staff supporting the Sydney Brain Tumour Bank in particular Mary Lordan, Jane Raffesath, Kristine Deang and Amy Lonergan. This research was enabled by access to facilities of The University of Sydney, including Sydney Analytical, Sydney Mass Spectrometry, and Sydney Microscopy and Microanalysis. A special thank you to Sydney Analytical staff, Dr Michelle Wood and Dr Elizabeth Carter for their invaluable support in acquiring and evaluating FT-IR data, and Dr Bhanu Mantri from Sydney Microscopy and Microanalysis for capturing cryo-transmission electron microscopy images. This work was supported by grants from SurFebruary Cancer Research Fund, Tour de Cure, Sydney Research, BF Foundation, James N Kirby Foundation and Cure My Brain.

CONFLICT OF INTEREST STATEMENT

The authors declare no competing interests.

ORCID

Hao-Wen Sim  <https://orcid.org/0000-0002-2530-0523>

Kimberley L. Alexander  <https://orcid.org/0000-0002-7239-039X>

REFERENCES

- Abbasi, A. W., Westerlaan, H. E., Holtman, G. A., Aden, K. M., van Laar, P. J., & van der Hoorn, A. (2018). Incidence of tumour progression and pseudoprogression in high-grade gliomas: A systematic review and meta-analysis. *Clinical Neuroradiology*, 28(3), 401–411.
- Abbastabar, M., Sarfi, M., Golestani, A., Karimi, A., Pourmand, G., & Khalili, E. (2020). Tumor-derived urinary exosomal long non-coding RNAs as diagnostic biomarkers for bladder cancer. *EXCLI Journal*, 19, 301–310.
- Ahmadzade, T., Vijayan, A., Vafae, F., Azimi, A., Reid, G., Clarke, S., Kao, S., Grau, G. E., & Hosseini-Beheshti, E. (2023). Small and large extracellular vesicles derived from pleural mesothelioma cell lines offer biomarker potential. *Cancers*, 15(8), 2364. <https://doi.org/10.3390/cancers15082364>
- Akers, J. C., Gonda, D., Kim, R., Carter, B. S., & Chen, C. C. (2013). Biogenesis of extracellular vesicles (EV): Exosomes, microvesicles, retrovirus-like vesicles, and apoptotic bodies. *Journal of Neuro-Oncology*, 113(1), 1–11.

- Akers, J. C., Ramakrishnan, V., Kim, R., Skog, J., Nakano, I., Pingle, S., Kalinina, J., Hua, W., Kesari, S., Mao, Y., Breakefield, X. O., Hochberg, F. H., Van Meir, E. G., Carter, B. S., & Chen, C. C. (2013). MiR-21 in the extracellular vesicles (EVs) of cerebrospinal fluid (CSF): A platform for glioblastoma biomarker development. *PLoS One*, 8(10), e78115.
- Alexandri, E., Ahmed, R., Siddiqui, H., Choudhary, M. I., Tsiafoulis, C. G., & Gerothanassis, I. P. (2017). High resolution NMR spectroscopy as a structural and analytical tool for unsaturated lipids in solution. *Molecules (Basel, Switzerland)*, 22(10), 1663. <https://doi.org/10.3390/molecules22101663>
- Ami, D., Mereghetti, P., & Doglia, S. M. (2013). Multivariate analysis for Fourier Transform Infrared Spectra of complex biological systems and processes. In L. Valim de Freitas, A. P. Barbosa & Rodrigues de Freitas (Eds.). *Multivariate analysis in management engineering and the sciences*. pp. 189–220.
- Amir, R. M., Anjum, F. M., Khan, M. I., Khan, M. R., Pasha, I., & Nadeem, M. (2013). Application of Fourier transform infrared (FTIR) spectroscopy for the identification of wheat varieties. *Journal of Food Science and Technology*, 50(5), 1018–1023.
- Ayre, D. C., Chute, I. C., Joy, A. P., Barnett, D. A., Hogan, A. M., Grüll, M. P., Peña-Castillo, L., Lang, A. S., Lewis, S. M., & Christian, S. L. (2017). CD24 induces changes to the surface receptors of B cell microvesicles with variable effects on their RNA and protein cargo. *Scientific Reports*, 7(1), 8642. <https://doi.org/10.1038/s41598-017-08094-8>
- Bao, Q., Huang, Q., Chen, Y., Wang, Q., Sang, R., Wang, L., Xie, Y., & Chen, W. (2021). Tumor-derived extracellular vesicles regulate cancer progression in the tumor microenvironment. *Frontiers in Molecular Biosciences*, 8, 796385.
- Blomme, A., Fahmy, K., Peulen, O., Costanza, B., Fontaine, M., Struman, I., Baiwir, D., de Pauw, E., Thiry, M., Bellahcène, A., Castronovo, V., & Turtoi, A. (2016). Myoferlin is a novel exosomal protein and functional regulator of cancer-derived exosomes. *Oncotarget*, 7(50), 83669–83683. <https://doi.org/10.18632/oncotarget.13276>
- Böselt, L., Aerts, R., Herrebout, W., & Riniker, S. (2023). Improving the IR spectra alignment algorithm with spectra deconvolution and combination with Raman or VCD spectroscopy. *Physical Chemistry Chemical Physics: PCCP*, 25(3), 2063–2074. <https://doi.org/10.1039/d2cp04907d>
- Bruschi, M., Granata, S., Santucci, L., Candiano, G., Fabris, A., Antonucci, N., Petretto, A., Bartolucci, M., Del Zotto, G., Antonini, F., Ghiggeri, G. M., Lupo, A., Gambaro, G., & Zaza, G. (2019). Proteomic analysis of urinary microvesicles and exosomes in medullary sponge kidney disease and autosomal dominant polycystic kidney disease. *Clinical Journal of the American Society of Nephrology: CJASN*, 14(6), 834–843.
- Brzozowski, J. S., Jankowski, H., Bond, D. R., McCague, S. B., Munro, B. R., Predebon, M. J., Scarlett, C. J., Skelding, K. A., & Weidenhofer, J. (2018). Lipidomic profiling of extracellular vesicles derived from prostate and prostate cancer cell lines. *Lipids in Health and Disease*, 17(1), 211. <https://doi.org/10.1186/s12944-018-0854-x>
- Bui, T. P., Le, P. L., Nguyen, L. T. T., Tho, L. T., & Trinh, T. H. (2022). Proteomic profiling of small extracellular vesicles isolated from the plasma of Vietnamese patients with non-small cell lung cancer reveals some potential biomarkers. *Asian Pacific Journal of Cancer Prevention*, 23(6), 1893–1900. <https://doi.org/10.31557/APJCP.2022.23.6.1893>
- Casati, G., Giunti, L., Iorio, A. L., Marturano, A., Galli, L., & Sardi, I. (2021). Hippo pathway in regulating drug resistance of glioblastoma. *International Journal of Molecular Sciences*, 22(24), 13431. <https://doi.org/10.3390/ijms222413431>
- Christy, A. A., & Egeberg, P. K. (2006). *Quantitative determination of saturated and unsaturated fatty acids in edible oils by infrared spectroscopy and chemometrics*. (Vol. 82(1–2), pp. 130–136) *Chemometrics and Intelligent Laboratory Systems. Classification of Tumours Editorial Board*. (2023). *Central nervous system tumours [Internet]. Lyon (France): International Agency for Research on Cancer; 2021 [cited 2023 07 23]. (WHO classification of tumours series, 5th ed.; vol. 6). https://tumourclassification.iarc.who.int/chapters/45*
- Cricri, G., Bellucci, L., Montini, G., & Collino, F. (2021). Urinary extracellular vesicles: uncovering the basis of the pathological processes in kidney-related diseases. *International Journal of Molecular Sciences*, 22(12), 6507.
- Davis, M. E. (2016). Glioblastoma: Overview of disease and treatment. *Clinical Journal of Oncology Nursing*, 20, (5 Suppl), S2–S8.
- Del Bene, M., Osti, D., Faletti, S., Beznoussenko, G. V., DiMeco, F., & Pelicci, G. (2022). Extracellular vesicles: The key for precision medicine in glioblastoma. *Neuro-oncology*, 24(2), 184–196.
- Derenne, A., Claessens, T., Conus, C., & Goormaghtigh, E. (2013). Infrared spectroscopy of membrane lipids. In G. C. K. Roberts (Ed.), *Encyclopedia of biophysics*. Springer. https://doi.org/10.1007/978-3-642-16712-6_558
- Di Santo, R., Vaccaro, M., Romanò, S., Di Giacinto, F., Papi, M., Rapaccini, G. L., De Spirito, M., Miele, L., Basile, U., & Ciasca, G. (2022). Machine learning-assisted FTIR analysis of circulating extracellular vesicles for cancer liquid biopsy. *Journal of Personalized Medicine*, 12(6), 949. <https://doi.org/10.3390/jpm12060949>
- Di Vizio, D., Morello, M., Dudley, A. C., Schow, P. W., Adam, R. M., Morley, S., Mulholland, D., Rotinen, M., Hager, M. H., Insabato, L., Moses, M. A., Demichelis, F., Lisanti, M. P., Wu, H., Klagsbrun, M., Bhowmick, N. A., Rubin, M. A., D'Souza-Schorey, C., & Freeman, M. R. (2012). Large oncosomes in human prostate cancer tissues and in the circulation of mice with metastatic disease. *The American Journal of Pathology*, 181(5), 1573–1584.
- Dragovic, R. A., Gardiner, C., Brooks, A. S., Tannetta, D. S., Ferguson, D. J., Hole, P., Carr, B., Redman, C. W., Harris, A. L., Dobson, P. J., Harrison, P., & Sargent, I. L. (2011). Sizing and phenotyping of circulating vesicles using nanoparticle tracking analysis. *Nanomedicine: Nanotechnology, Biology, and Medicine*, 7(6), 780–788.
- Ebrahimkhani, S., Vafaee, F., Hallal, S., Wei, H., Lee, M. Y. T., Young, P. E., Satgunaseelan, L., Beadnall, H., Barnett, M. H., Shivalingam, B., Suter, C. M., Buckland, M. E., & Kaufman, K. L. (2018). Deep sequencing of circulating exosomal microRNA allows non-invasive glioblastoma diagnosis. *NPJ Precision Oncology*, 2, 28.
- Eisenberg, M. C., Kim, Y., Li, R., Ackerman, W. E., Kniss, D. A., & Friedman, A. (2011). Mechanistic modeling of the effects of myoferlin on tumor cell invasion. *Proceedings of the National Academy of Sciences of the United States of America*, 108(50), 20078–20083. <https://doi.org/10.1073/pnas.1116327108>
- Erdbrügger, U., Blijdorp, C. J., Bijnsdorp, I. V., Borràs, F. E., Burger, D., Bussolati, B., Byrd, J. B., Clayton, A., Dear, J. W., Falcón-Pérez, J. M., Grange, C., Hill, A. F., Holthöfer, H., Hoorn, E. J., Jenster, G., Jimenez, C. R., Junker, K., Klein, J., Knepper, M. A., ... Martens-Uzunova, E. S. (2021). Urinary extracellular vesicles: A position paper by the urine task force of the international society for extracellular vesicles. *Journal of Extracellular Vesicles*, 10(7), e12093.
- Erdbrügger, U., Blijdorp, C. J., Bijnsdorp, I. V., Borràs, F. E., Burger, D., Bussolati, B., Byrd, J. B., Clayton, A., Dear, J. W., Falcón-Pérez, J. M., Grange, C., Hill, A. F., Holthöfer, H., Hoorn, E. J., Jenster, G., Jimenez, C. R., Junker, K., Klein, J., Knepper, M. A., ... Martens-Uzunova, E. S. (2021). Urinary extracellular vesicles: A position paper by the urine task force of the international society for extracellular vesicles. *Journal of Extracellular Vesicles*, 10(7), e12093.
- Erdbrügger, U., & Le, T. H. (2016). Extracellular vesicles in renal diseases: More than novel biomarkers?. *Journal of the American Society of Nephrology: JASN*, 27(1), 12–26.
- Fernández-Llana, P., Khosrith, S., Gonzales, P. A., Star, R. A., Pisitkun, T., & Knepper, M. A. (2010). Tamm-Horsfall protein and urinary exosome isolation. *Kidney International*, 77(8), 736–742.
- Finnerty, C. C., Mabvuure, N. T., Ali, A., Kozar, R. A., & Herndon, D. N. (2013). The surgically induced stress response. *Journal of Parenteral and Enteral Nutrition*, 37(Suppl 5), 21S–29S. <https://doi.org/10.1177/0148607113496117>
- Fraser, K. B., Rawlins, A. B., Clark, R. G., Alcalay, R. N., Standaert, D. G., Liu, N., Parkinson's Disease Biomarker Program Consortium, & West, A. B. (2016). Ser(P)-1292 LRRK2 in urinary exosomes is elevated in idiopathic Parkinson's disease. *Movement Disorders: Official Journal of the Movement Disorder Society*, 31(10), 1543–1550.

- Furukawa, R., Homma, H., Inoue, T., Horiuchi, H., & Usui, K. (2018). Cytomegalovirus hemorrhagic cystitis in a malignant glioma patient treated with temozolomide. *Internal Medicine, (Tokyo, Japan)*, 57(20), 3047–3050. <https://doi.org/10.2169/internalmedicine.1005-18>
- Gillet, L. C., Navarro, P., Tate, S., Röst, H., Selevsek, N., Reiter, L., Bonner, R., & Aebersold, R. (2012). Targeted data extraction of the MS/MS spectra generated by data-independent acquisition: A new concept for consistent and accurate proteome analysis. *Molecular & Cellular Proteomics*, 11(6), O111.016717.
- Hallal, S., Azimi, A., Wei, H., Ho, N., Lee, M. Y. T., Sim, H. W., Sy, J., Shivalingam, B., Buckland, M. E., & Alexander-Kaufman, K. L. (2020). A comprehensive proteomic SWATH-MS workflow for profiling blood extracellular vesicles: A new avenue for glioma tumour surveillance. *International Journal of Molecular Sciences*, 21(13), 4754.
- Hallal, S., Ebrahimkhani, S., Shivalingam, B., Graeber, M. B., Kaufman, K. L., & Buckland, M. E. (2019). The emerging clinical potential of circulating extracellular vesicles for non-invasive glioma diagnosis and disease monitoring. *Brain Tumor Pathology*, 36(2), 29–39.
- Hallal, S., Ebrahim Khani, S., Wei, H., Lee, M. Y. T., Sim, H. W., Sy, J., Shivalingam, B., Buckland, M. E., & Alexander-Kaufman, K. L. (2020). Deep sequencing of small RNAs from neurosurgical extracellular vesicles substantiates miR-486-3p as a circulating biomarker that distinguishes glioblastoma from lower-grade astrocytoma patients. *International Journal of Molecular Sciences*, 21(14), 4954.
- Hallal, S., Russell, B. P., Wei, H., Lee, M. Y. T., Toon, C. W., Sy, J., Shivalingam, B., Buckland, M. E., & Kaufman, K. L. (2019). Extracellular vesicles from neurosurgical aspirates identifies chaperonin containing TCP1 subunit 6A as a potential glioblastoma biomarker with prognostic significance. *Proteomics*, 19(1–2), e1800157.
- Hallal, S., Túzesi, Á., Grau, G. E., Buckland, M. E., & Alexander, K. L. (2022). Understanding the extracellular vesicle surface for clinical molecular biology. *Journal of Extracellular Vesicles*, 11(10), e12260. <https://doi.org/10.1002/jev.12260>
- Hallal, S. M., Túzesi, Á., Sida, L. A., Xian, E., Madani, D., Muralidharan, K., Shivalingam, B., Buckland, M. E., Satgunaseelan, L., & Alexander, K. L. (2024). Glioblastoma biomarkers in urinary extracellular vesicles reveal the potential for a ‘liquid gold’ biopsy. *British Journal of Cancer*, 130(5), 836–851.
- Haraszti, R. A., Didiot, M. C., Sapp, E., Leszyk, J., Shaffer, S. A., Rockwell, H. E., Gao, F., Narain, N. R., DiFiglia, M., Kiebish, M. A., Aronin, N., & Khvorova, A. (2016). High-resolution proteomic and lipidomic analysis of exosomes and microvesicles from different cell sources. *Journal of Extracellular Vesicles*, 5, 32570. <https://doi.org/10.3402/jev.v5.32570>
- Hayashi, N., Doi, H., Kurata, Y., Kagawa, H., Atobe, Y., Funakoshi, K., Tada, M., Katsumoto, A., Tanaka, K., Kunii, M., Nakamura, H., Takahashi, K., Takeuchi, H., Koyano, S., Kimura, Y., Hirano, H., & Tanaka, F. (2020). Proteomic analysis of exosome-enriched fractions derived from cerebrospinal fluid of amyotrophic lateral sclerosis patients. *Neuroscience Research*, 160, 43–49. <https://doi.org/10.1016/j.neures.2019.10.010>
- Hendriks, R. J., Dijkstra, S., Jannink, S. A., Steffens, M. G., van Oort, I. M., Mulders, P. F., & Schalken, J. A. (2016). Comparative analysis of prostate cancer specific biomarkers PCA3 and ERG in whole urine, urinary sediments and exosomes. *Clinical Chemistry and Laboratory Medicine*, 54(3), 483–492. <https://doi.org/10.1515/cclm-2015-0599>
- Hirschfeld, M., Rücker, G., Weiß, D., Berner, K., Ritter, A., Jäger, M., & Erbes, T. (2020). Urinary exosomal MicroRNAs as potential non-invasive biomarkers in breast cancer detection. *Molecular Diagnosis & Therapy*, 24(2), 215–232.
- Ju, J., Zhang, H., Lin, M., Yan, Z., An, L., Cao, Z., Geng, D., Yue, J., Tang, Y., Tian, L., Chen, F., Han, Y., Wang, W., Zhao, S., Jiao, S., & Zhou, Z. (2024). The alanyl-tRNA synthetase AARS1 moonlights as a lactyltransferase to promote YAP signaling in gastric cancer. *The Journal of Clinical Investigation*, 134(10), e174587. <https://doi.org/10.1172/JCI174587>
- Kalra, H., Drummen, G. P., & Mathivanan, S. (2016). Focus on extracellular vesicles: Introducing the next small big thing. *International Journal of Molecular Sciences*, 17(2), 170. <https://doi.org/10.3390/ijms17020170>
- Karpmann, D., Ståhl, A. L., & Arvidsson, I. (2017). Extracellular vesicles in renal disease. *Nature Reviews Nephrology*, 13(9), 545–562.
- Kerjaschki, D., Schulze, M., Binder, S., Kain, R., Ojha, P. P., Susani, M., Horvat, R., Baker, P. J., & Couser, W. G. (1989). Transcellular transport and membrane insertion of the C5b-9 membrane attack complex of complement by glomerular epithelial cells in experimental membranous nephropathy. *Journal of Immunology (Baltimore, Md.: 1950)*, 143(2), 546–552.
- Kosti, A., de Araujo, P. R., Li, W. Q., Guardia, G. D. A., Chiou, J., Yi, C., Ray, D., Meliso, F., Li, Y. M., Delambre, T., Qiao, M., Burns, S. S., Lorbeer, F. K., Georgi, F., Flosbach, M., Klinnert, S., Jenseit, A., Lei, X., Sandoval, C. R., ... Penalva, L. O. F. (2020). The RNA-binding protein SERBP1 functions as a novel oncogenic factor in glioblastoma by bridging cancer metabolism and epigenetic regulation. *Genome Biology*, 21(1), 195. <https://doi.org/10.1186/s13059-020-02115-y>
- Kou, Y., Geng, F., & Guo, D. (2022). Lipid metabolism in glioblastoma: From de novo synthesis to storage. *Biomedicines*, 10(8), 1943. <https://doi.org/10.3390/biomedicines10081943>
- Lewis, R. N., & McElhaney, R. N. (2013). Membrane lipid phase transitions and phase organization studied by Fourier transform infrared spectroscopy. *Biochimica Et Biophysica Acta*, 1828(10), 2347–2358. <https://doi.org/10.1016/j.bbamem.2012.10.018>
- Li, Y., Zhang, Y., Qiu, F., & Qiu, Z. (2011). Proteomic identification of exosomal LRG1: A potential urinary biomarker for detecting NSCLC. *Electrophoresis*, 32(15), 1976–1983.
- Liao, Z., Ke, W., Liu, H., Tong, B., Wang, K., Feng, X., Hua, W., Wang, B., Song, Y., Luo, R., Liang, H., Zhang, W., Zhao, K., Li, S., & Yang, C. (2022). Vasin-containing small extracellular vesicles retard intervertebral disc degeneration utilizing an injectable thermoresponsive delivery system. *Journal of Nanobiotechnology*, 20(1), 420. <https://doi.org/10.1186/s12951-022-01624-1>
- Liu, Z., Yee, P. P., Wei, Y., Liu, Z., Kawasaki, Y. I., & Li, W. (2019). Differential YAP expression in glioma cells induces cell competition and promotes tumorigenesis. *Journal of Cell Science*, 132(5), jcs225714. <https://doi.org/10.1242/jcs.225714>
- Londono, I., & Bendayan, M. (2005). Glomerular handling of native albumin in the presence of circulating modified albumins by the normal rat kidney. *American Journal of Physiology-Renal Physiology*, 289(6), F1201–F1209.
- Ma, L., Li, Y., Peng, J., Wu, D., Zhao, X., Cui, Y., Chen, L., Yan, X., Du, Y., & Yu, L. (2015). Discovery of the migrasome, an organelle mediating release of cytoplasmic contents during cell migration. *Cell Research*, 25(1), 24–38.
- Mallawaarachy, D. M., Hallal, S., Russell, B., Ly, L., Ebrahimkhani, S., Wei, H., Christopherson, R. I., Buckland, M. E., & Kaufman, K. L. (2017). Comprehensive proteome profiling of glioblastoma-derived extracellular vesicles identifies markers for more aggressive disease. *Journal of Neuro-Oncology*, 131(2), 233–244. <https://doi.org/10.1007/s11060-016-2298-3>
- Mao, Y. K., Liu, Z. B., & Cai, L. (2020). Identification of glioblastoma-specific prognostic biomarkers via an integrative analysis of DNA methylation and gene expression. *Oncology Letters*, 20(2), 1619–1628. <https://doi.org/10.3892/ol.2020.11729>
- Mastronarde, D. N. (2005). Automated electron microscope tomography using robust prediction of specimen movements. *Journal of Structural Biology*, 152(1), 36–51.
- Melentijevic, I., Toth, M. L., Arnold, M. L., Guasp, R. J., Harinath, G., Nguyen, K. C., Taub, D., Parker, J. A., Neri, C., Gabel, C. V., Hall, D. H., & Driscoll, M. (2017). C. elegans neurons jettison protein aggregates and mitochondria under neurotoxic stress. *Nature*, 542(7641), 367–371.
- Merchant, M. L., Rood, I. M., Deegens, J. K. J., & Klein, J. B. (2017). Isolation and characterization of urinary extracellular vesicles: Implications for biomarker discovery. *Nature Reviews. Nephrology*, 13(12), 731–749. <https://doi.org/10.1038/nrneph.2017.148>

- Mihály, J., Deák, R., Szigyártó, I. C., Bóta, A., Beke-Somfai, T., & Varga, Z. (2017). Characterization of extracellular vesicles by IR spectroscopy: Fast and simple classification based on amide and CH stretching vibrations. *Biochimica Et Biophysica Acta. Biomembranes*, 1859(3), 459–466. <https://doi.org/10.1016/j.bbmem.2016.12.005>
- Movasaghi, Z., Rehman, S., & ur Rehman, D. R. I. (2008). Fourier transform infrared (FTIR) spectroscopy of biological tissues. *Applied Spectroscopy Reviews*, 43(2), 134–179.
- Musante, L., Bontha, S. V., La Salvia, S., Fernandez-Piñeros, A., Lannigan, J., Le, T. H., Mas, V., & Erdbrügger, U. (2020). Rigorous characterization of urinary extracellular vesicles (uEVs) in the low centrifugation pellet—A neglected source for uEVs. *Scientific Reports*, 10(1), 3701.
- Naumann, D. (2001). FT-infrared and FT-Raman spectroscopy in biomedical research. *Applied Spectroscopy Reviews*, 36(2–3), 239–298.
- Ndisang, J. F. (2018). Glomerular endothelium and its impact on glomerular filtration barrier in diabetes: Are the gaps still illusive? *Current Medicinal Chemistry*, 25(13), 1525–1529.
- Paolino, G., Buratta, S., Mercuri, S. R., Pellegrino, R. M., Urbanelli, L., Emiliani, C., Bertuccini, L., Iosi, F., Huber, V., Brianti, P., Prezioso, C., Di Nicola, M. R., Federici, C., & Lugini, L. (2022). Lipidic profile changes in exosomes and microvesicles derived from plasma of monoclonal antibody-treated psoriatic patients. *Frontiers in Cell and Developmental Biology*, 10, 923769. <https://doi.org/10.3389/fcell.2022.923769>
- Pathan, M., Keerthikumar, S., Ang, C. S., Gangoda, L., Quek, C. Y., Williamson, N. A., Mouradov, D., Sieber, O. M., Simpson, R. J., Salim, A., Bacic, A., Hill, A. F., Stroud, D. A., Ryan, M. T., Agbinya, J. I., Mariadason, J. M., Burgess, A. W., & Mathivanan, S. (2015). FunRich: An open access standalone functional enrichment and interaction network analysis tool. *Proteomics*, 15(15), 2597–2601. <https://doi.org/10.1002/pmic.201400515>
- Patrakka, J., Lahdenkari, A. T., Koskimies, O., Holmberg, C., Wartiovaara, J., & Jalanko, H. (2002). The number of podocyte slit diaphragms is decreased in minimal change nephrotic syndrome. *Pediatric Research*, 52(3), 349–355.
- Pavlyukov, M. S., Yu, H., Bastola, S., Minata, M., Shender, V. O., Lee, Y., Zhang, S., Wang, J., Komarova, S., Wang, J., Yamaguchi, S., Alsheikh, H. A., Shi, J., Chen, D., Mohyeldin, A., Kim, S. H., Shin, Y. J., Anufrieva, K., Evtushenko, E. G., ... Nakano, I. (2018). Apoptotic cell-derived extracellular vesicles promote malignancy of glioblastoma via intercellular transfer of splicing factors. *Cancer Cell*, 34(1), 119–135.e 10.
- Perez-Riverol, Y., Bai, J., Bandla, C., García-Seisdedos, D., Hewapathirana, S., Kamatchinathan, S., Kundu, D. J., Prakash, A., Frericks-Zipper, A., Eisenacher, M., Walzer, M., Wang, S., Brazma, A., & Vizcaino, J. A. (2022). The PRIDE database resources in 2022: A hub for mass spectrometry-based proteomics evidences. *Nucleic Acids Research*, 50(D1), D543–D552. <https://doi.org/10.1093/nar/gkabi038>
- Peychl, L., & Zalud, R. (2008). Zmeny v mocovém mechýři po krátkodobém zavedení permanentního katétru [Changes in the urinary bladder caused by short-term permanent catheter insertion]. *Casopis Lekarů Ceských*, 147(6), 325–329.
- Polisetty, R. V., Gautam, P., Sharma, R., Harsha, H. C., Nair, S. C., Gupta, M. K., Uppin, M. S., Challa, S., Puligopu, A. K., Ankathi, P., Purohit, A. K., Chandak, G. R., Pandey, A., & Sirdeshmukh, R. (2012). LC-MS/MS analysis of differentially expressed glioblastoma membrane proteome reveals altered calcium signaling and other protein groups of regulatory functions. *Molecular & Cellular Proteomics*, 11(6), M111.013565. <https://doi.org/10.1074/mcp.M111.013565>
- Portaccio, M., Faramarzi, B., & Lepore, M. (2023). Probing biochemical differences in lipid components of human cells by means of ATR-FTIR spectroscopy. *Biophysica*, 3(3), 524–538.
- Quezada, C., Torres, Á., Niechi, I., Uribe, D., Contreras-Duarte, S., Toledo, F., San Martín, R., Gutiérrez, J., & Sobrevia, L. (2018). Role of extracellular vesicles in glioma progression. *Molecular Aspects of Medicine*, 60, 38–51.
- Raimondo, F., Chinello, C., Stella, M., Santorelli, L., Magni, F., & Pitto, M. (2018). Effects of hematuria on the proteomic profile of urinary extracellular vesicles: Technical challenges. *Journal of Proteome Research*, 17(8), 2572–2580. <https://doi.org/10.1021/acs.jproteome.7b00763>
- Romano, S., Di Giacinto, F., Primiano, A., Mazzini, A., Panzetta, C., Papi, M., Di Gaspare, A., Ortolani, M., Gervasoni, J., De Spirito, M., Nocca, G., & Ciasca, G. (2020). Fourier Transform Infrared Spectroscopy as a useful tool for the automated classification of cancer cell-derived exosomes obtained under different culture conditions. *Analytica Chimica Acta*, 1140, 219–227. <https://doi.org/10.1016/j.aca.2020.09.037>
- Rose, G. D. (2004). *Secondary structure in protein analysis, in encyclopedia of biological chemistry* (pp. 1–6) W. J. Lennarz & M. D. Lane (Eds.), Elsevier.
- Saha, S. K., Choi, H. Y., Kim, B. W., Dayem, A. A., Yang, G. M., Kim, K. S., Yin, Y. F., & Cho, S. G. (2017). KRT19 directly interacts with β -catenin/RAC1 complex to regulate NUMB-dependent NOTCH signaling pathway and breast cancer properties. *Oncogene*, 36(3), 332–349. <https://doi.org/10.1038/ncr.2016.221>
- Sonoda, H., Lee, B. R., Park, K. H., Nihalani, D., Yoon, J. H., Ikeda, M., & Kwon, S. H. (2019). miRNA profiling of urinary exosomes to assess the progression of acute kidney injury. *Scientific Reports*, 9(1), 4692.
- Sottoriva, A., Spiteri, I., Piccirillo, S. G., Touloumis, A., Collins, V. P., Marioni, J. C., Curtis, C., Watts, C., & Tavaré, S. (2013). Intratumor heterogeneity in human glioblastoma reflects cancer evolutionary dynamics. *Proceedings of the National Academy of Sciences of the United States of America*, 110(10), 4009–4014.
- Soylemez, B., Bulut, Z., & Şahin-Böllükbaşı, S. (2023). Investigating the potential of lipids for use as biomarkers for glioblastoma via an untargeted lipidomics approach. *Journal of Korean Neurosurgical Society*, 66(2), 133–143. <https://doi.org/10.3340/jkns.2022.0091>
- Stępień, E. Ł., Kamińska, A., Surman, M., Karbowska, D., Wróbel, A., & Przybyło, M. (2021). Fourier-Transform InfraRed (FT-IR) spectroscopy to show alterations in molecular composition of EV subpopulations from melanoma cell lines in different malignancy. *Biochemistry and Biophysics Reports*, 25, 100888. <https://doi.org/10.1016/j.bbrep.2020.100888>
- Street, J. M., Barran, P. E., Mackay, C. L., Weidt, S., Balmforth, C., Walsh, T. S., Chalmers, R. T., Webb, D. J., & Dear, J. W. (2012). Identification and proteomic profiling of exosomes in human cerebrospinal fluid. *Journal of Translational Medicine*, 10, 5.
- Sun, R., Wang, H., Shi, Y., Gao, D., Sun, Z., Chen, Z., Jiang, H., & Zhang, J. (2019). A pilot study of urinary exosomes in Alzheimer's disease. *Neuro-degenerative Diseases*, 19(5–6), 184–191.
- Théry, C., Witwer, K. W., Aikawa, E., Alcaraz, M. J., Anderson, J. D., Andriantsitohaina, R., Antoniou, A., Arab, T., Archer, F., Atkin-Smith, G. K., Ayre, D. C., Bach, J. M., Bachurski, D., Baharvand, H., Balaj, L., Baldacchino, S., Bauer, N. N., Baxter, A. A., Bebawy, M., ... Zuba-Surma, E. K. (2018). Minimal information for studies of extracellular vesicles 2018 (MISEV2018): A position statement of the International Society for Extracellular Vesicles and update of the MISEV2014 guidelines. *Journal of Extracellular Vesicles*, 7(1), 1535750.
- Tian, T., Li, A., Lu, H., Luo, R., Zhang, M., & Li, Z. (2015). TAZ promotes temozolomide resistance by upregulating MCL-1 in human glioma cells. *Biochemical and Biophysical Research Communications*, 463(4), 638–643. <https://doi.org/10.1016/j.bbrc.2015.05.115>
- Tkac, M., Kowal, J., & Théry, C. (2018). Why the need and how to approach the functional diversity of extracellular vesicles. *Philosophical Transactions of the Royal Society of London. Series B, Biological Sciences*, 373(1737), 20160479. <https://doi.org/10.1098/rstb.2016.0479>
- Tyanova, S., Temu, T., Sinitcyn, P., Carlson, A., Hein, M. Y., Geiger, T., Mann, M., & Cox, J. (2016). The Perseus computational platform for comprehensive analysis of (prote)omics data. *Nature Methods*, 13(9), 731–740. <https://doi.org/10.1038/nmeth.3901>
- Uthamacumaran, A., Elouatik, S., Abdouh, M., Berteau-Rainville, M., Gao, Z. H., & Arena, G. (2022). Machine learning characterization of cancer patients-derived extracellular vesicles using vibrational spectroscopies: Results from a pilot study. *Applied Intelligence*, 52(11), 12737–12753.

- Vagner, T., Spinelli, C., Minciacchi, V. R., Balaj, L., Zandian, M., Conley, A., Zijlstra, A., Freeman, M. R., Demichelis, F., De, S., Posadas, E. M., Tanaka, H., & Di Vizio, D. (2018). Large extracellular vesicles carry most of the tumour DNA circulating in prostate cancer patient plasma. *Journal of Extracellular Vesicles*, 7(1), 1505403.
- Vitale, S. R., Helmijr, J. A., Gerritsen, M., Coban, H., van Dessel, L. F., Beije, N., van der Vlugt-Daane, M., Vigneri, P., Sieuwerts, A. M., Dits, N., van Royen, M. E., Jenster, G., Sleijfer, S., Lolkema, M., & Jansen, M. P. H. M. (2021). Detection of tumor-derived extracellular vesicles in plasma from patients with solid cancer. *BMC Cancer*, 21(1), 315. <https://doi.org/10.1186/s12885-021-08007-z>
- Wang, S., Kojima, K., Mobley, J. A., & West, A. B. (2019). Proteomic analysis of urinary extracellular vesicles reveal biomarkers for neurologic disease. *EBioMedicine*, 45, 351–361.
- Welsh, J. A., Goberdhan, D. C. I., O'Driscoll, L., Buzas, E. I., Blenkiron, C., Bussolati, B., Cai, H., Di Vizio, D., Driedonks, T. A. P., Erdbrügger, U., Falcon-Perez, J. M., Fu, Q. L., Hill, A. F., Lenassi, M., Lim, S. K., Mahoney, M. G., Mohanty, S., Möller, A., Nieuwland, R., ... Witwer, K. W. (2024). Minimal information for studies of extracellular vesicles (MISEV2023): From basic to advanced approaches. *Journal of Extracellular Vesicles*, 13(2), e12404.
- Xavier, C. P. R., Cairnes, H. R., Barbosa, M. A. G., Bergantim, R., Guimarães, J. E., & Vasconcelos, M. H. (2020). The role of extracellular vesicles in the hallmarks of cancer and drug resistance. *Cells*, 9(5), 1141.
- Xu, J., Fang, J., Cheng, Z., Fan, L., Hu, W., Zhou, F., & Shen, H. (2018). Overexpression of the Kininogen-1 inhibits proliferation and induces apoptosis of glioma cells. *Journal of Experimental & Clinical Cancer Research: CR*, 37(1), 180. <https://doi.org/10.1186/s13046-018-0833-0>
- Yang, N., Li, S., Li, G., Zhang, S., Tang, X., Ni, S., Jian, X., Xu, C., Zhu, J., & Lu, M. (2017). The role of extracellular vesicles in mediating progression, metastasis and potential treatment of hepatocellular carcinoma. *Oncotarget*, 8(2), 3683–3695. <https://doi.org/10.18632/oncotarget.12465>
- Yap, X. L., Ong, T. A., Lim, J., Wood, B., & Lee, W. L. (2019). Study of prostate cancer-derived extracellular vesicles in urine using IR spectroscopy. *Progress in Drug Discovery & Biomedical Science*, 2(1), 00–00.
- Yekula, A., Minciacchi, V. R., Morello, M., Shao, H., Park, Y., Zhang, X., Muralidharan, K., Freeman, M. R., Weissleder, R., Lee, H., Carter, B., Breakefield, X. O., Di Vizio, D., & Balaj, L. (2019). Large and small extracellular vesicles released by glioma cells *in vitro* and *in vivo*. *Journal of Extracellular Vesicles*, 9(1), 1689784. <https://doi.org/10.1080/20013078.2019.1689784>
- Yu, N., & Aboud, O. (2024). The lipidomic signature of glioblastoma: A promising frontier in cancer research. *Cancers*, 16(6), 1089. <https://doi.org/10.3390/cancers16061089>
- Yuan, Q., Zuo, F. X., Cai, H. Q., Qian, H. P., & Wan, J. H. (2022). Identifying differential expression genes and prognostic signature based on subventricular zone involved glioblastoma. *Frontiers in genetics*, 13, 912227. <https://doi.org/10.3389/fgene.2022.912227>
- Zhai, C., Xie, F., Xu, J., Yang, Y., Zheng, W., Hu, H., Ding, X., & Yu, H. (2023). Correlation between membrane proteins and sizes of extracellular vesicles and particles: A potential signature for cancer diagnosis. *Journal of Extracellular Vesicles*, 12(12), e12391. <https://doi.org/10.1002/jev2.12391>
- Zhang, H., & Lyden, D. (2019). Asymmetric-flow field-flow fractionation technology for exomere and small extracellular vesicle separation and characterization. *Nature Protocols*, 14(4), 1027–1053. <https://doi.org/10.1038/s41596-019-0126-x>
- Zhang, Q., Jeppesen, D. K., Higginbotham, J. N., Graves-Deal, R., Trinh, V. Q., Ramirez, M. A., Sohn, Y., Neining, A. C., Taneja, N., McKinley, E. T., Niitsu, H., Cao, Z., Evans, R., Glass, S. E., Ray, K. C., Fissell, W. H., Hill, S., Rose, K. L., Huh, W. J., ... Coffey, R. J. (2021). Supermeres are functional extracellular nanoparticles replete with disease biomarkers and therapeutic targets. *Nature Cell Biology*, 23(12), 1240–1254. <https://doi.org/10.1038/s41556-021-00805-8>
- Zikou, A., Sioka, C., Alexiou, G. A., Fotopoulos, A., Voulgaris, S., & Argyropoulou, M. I. (2018). Radiation necrosis, pseudoprogression, pseudoresponse, and tumor recurrence: Imaging challenges for the evaluation of treated gliomas. *Contrast Media & Molecular Imaging*, 2018, 6828396.
- Zong, Z., Xie, F., Wang, S., Wu, X., Zhang, Z., Yang, B., & Zhou, F. (2024). Alanyl-tRNA synthetase, AARS1, is a lactate sensor and lactyltransferase that lactylates p53 and contributes to tumorigenesis. *Cell*, 187(10), 2375–2392.e33. <https://doi.org/10.1016/j.cell.2024.04.002>

SUPPORTING INFORMATION

Additional supporting information can be found online in the Supporting Information section at the end of this article.

How to cite this article: Hallal, S. M., Sida, L. A., Túzesi, C. Á., Shivalingam, B., Sim, H.-W., Buckland, M. E., Satgunaseelan, L., & Alexander, K. L. (2024). Size matters: Biomolecular compositions of small and large extracellular vesicles in the urine of glioblastoma patients. *Journal of Extracellular Biology*, 3, e70021. <https://doi.org/10.1002/jex2.70021>